nature communications

Article

https://doi.org/10.1038/s41467-026-70583-0

INSIG1/2 succination mediated by the moonlighting function of ADSL promotes lipogenesis and liver tumorigenesis

Received: 2 August 2024

Accepted: 3 March 2026

Published online: 15 March 2026

Check for updates

Yuran Duan[1,2,3,4,14], Shuo Wang[5,14], Jianyu Liu[6,7,14], Wenxing Qin[8,9,10,14], Yuli Shen[1,2,14], Yueru Hou[1,2], Xue Sun[6], Yanni Lin[1,2], Zhiqiang Hu[1,2], Bofei Dong[1,2], Yanli Bi[3,4], Huang Yang[11], Min Li[1,2], Liwei Xiao[1,2], Qingang Wu[1,2], Xueli Bai[1], Yuhao Wang[1], Gaopeng Li[12], Yuan Ding[3,4], Zhengwei Mao[11], Yang Luo[13], Zhimin Lu[1,2], Tong Liu[6,7], Daqian Xu[1,2,7] ✉, Shijian Liu[6] ✉, Peng Zhan[5] ✉ & Zheng Wang[1,2] ✉

Aerobic glycolysis supports tumor growth, but how tumor cells sense glucose to coordinate biosynthesis remains largely unclear. Here we show that in hepatocellular carcinoma cells, glucose-activated PKCε phosphorylates the purine synthesis enzyme ADSL, triggering its translocation to the endoplasmic reticulum. ADSL then promotes succination of INSIG1/2, which disrupts the interaction between INSIG proteins and SCAP, leading to the translocation of the SCAP-SREBP complex to the Golgi, the activation of SREBP-1 and the transcription of downstream lipogenesis-related genes, proliferation of tumor cells, and tumorigenesis in mice. Through virtual screening, we identify Elsulfavirine, an approved HIV drug, which blocks ADSL-INSIG interaction and suppresses SREBP-1 activation induced by glucose. Combining Elsulfavirine with Lenvatinib synergistically inhibits tumor growth. Clinically, ADSL phosphorylation and INSIG succination correlate with SREBP-1 activation and poor prognosis in human HCC. In summary, these findings reveal a repurposing mechanism by which tumor cells coordinate glucose metabolism and lipogenesis via a moonlighting function of ADSL and underscore a repurposing strategy for liver cancer therapy.

The ability of cancer cells to rewire their metabolism and energy transduction networks to support rapid proliferation has been well documented[1,2]. An increase in lipid metabolism is a remarkable feature of cancer metabolism[3]. Sterol regulatory element-binding proteins (SREBPs) are the key transcription factors responsible for the expression of most of enzymes involved in de novo lipogenesis and cholesterol biosynthesis. In mammals, two SREBP genes exist: *SREBF1* and *SREBF2*[4]. SREBP-1a and SREBP-1c, derived from *SREBF1* with distinct N-termini (20 amino acids), predominantly regulate genes crucial for fatty acid biosynthesis. In contrast, SREBP-2, encoded by *SREBF2*, orchestrates cholesterol synthesis. SREBP-1 and SREBP-2 are produced as inactive precursors that are attached to the membrane of the endoplasmic reticulum (ER), where they bind to two other proteins, sterol regulatory element-binding protein cleavage-activating protein (SCAP) and insulin-induced gene (INSIG)[5]. This complex is stabilized by the binding of INSIG to oxysterols. When cellular cholesterol and oxysterol levels are low, the SCAP-SREBP complex separates from INSIG and moves from the ER to the Golgi apparatus, where SREBP is cleaved by two membrane-bound proteases[5–7]. Subsequently, the released N-terminal segment of SREBP migrates to the nucleus and

A full list of affiliations appears at the end of the paper. ✉e-mail: xudaqian@zju.edu.cn; liushijian@hrbmu.edu.cn; zhanpeng1982@sdu.edu.cn; wangzheng22@zju.edu.cn

initiates the expression of genes involved in lipogenesis[8]. A link between SREBP-1 activation and the glucose supply has been reported under both physiological and pathophysiological conditions[9–12]. While glucose serves as a major resource for de novo lipid synthesis, the mechanism by which it regulates SREBP-1 activation remains largely unclear.

Adenylosuccinate lyase (ADSL) is an enzyme involved in de novo purine synthesis. It catalyzes two reactions: the conversion of succinylaminoimidazole carboxamide ribotide (SAICAR) to aminoimidazole carboxamide ribotide (AICAR) and fumarate, and the conversion of adenylosuccinate (also known as succinyladenosine monophosphate, S-AMP) to adenosine monophosphate (AMP) and fumarate[13,14]. Fumarate has been shown to function as an oncometabolite capable of eliciting epigenetic modifications by inhibiting α-ketoglutarate-dependent dioxygenases responsible for DNA and histone demethylation[15,16]. In addition, fumarate acts as an endogenous electrophile that undergoes spontaneous Michael addition reactions with cysteine sulfhydryl groups under physiological conditions[17]. This non-enzymatic reaction forms irreversible thioester linkages, generating S-(2-succino)cysteine (2SC)—a process termed succination[17]. Thus, succination represents an irreversible post-translational modification mediated through Michael addition chemistry between fumarate and cysteine residues. Fumarate promotes the succination of Kelch-like ECH-associated protein 1 (KEAP1), leading to the disruption of its interaction with nuclear factor (erythroid-derived 2)-like 2 (NRF2) and subsequent NRF2-mediated antioxidant gene expression[18]. In addition, fumarate has also been identified as an immunomodulator for its succination of glyceraldehyde-3-phosphate dehydrogenase (GAPDH) and gasdermin D[19,20]. However, whether the fumarate produced by ADSL, a vital enzyme in de novo purine synthesis, can reprogram tumor metabolism and tumorigenesis through a moonlighting function has not been determined. Additionally, how cancer cells couple multiple macromolecular synthetic processes, such as lipogenesis and nucleotide biosynthesis, to sustain enhanced bioenergetic homeostasis vital for cancer cell survival remains poorly understood.

In this report, we show that glucose levels regulate the phosphorylation of ADSL via protein kinase C epsilon (PKCε). Phosphorylated ADSL binds to INSIG1/2, resulting in INSIG1/2 succination, disassociation of oxysterols from INSIG1/2, activation of SREBPs, and subsequently enhanced lipogenesis. Inhibition of the interaction between ADSL and INSIG1/2 by the HIV non-nucleoside reverse transcriptase inhibitor (NNRTI) Elsulfavirine inhibits liver tumor growth.

Results

ADSL phosphorylated by PKCε translocates to the ER and binds to INSIG1/2

Tumor cells exhibit high glucose uptake and lactate production regardless of oxygen levels, a phenomenon known as the Warburg effect[21,22]. We immunoprecipitated INSIG1 (Fig. 1a) and INSIG2 (Supplementary Fig. 1a) from Huh7 human hepatocellular carcinoma (HCC) cells cultured in high-glucose medium to determine how tumor cells respond to high glucose and initiate lipogenesis. Mass spectrometric analyses of the immunoprecipitates identified ADSL as an associated protein under high-glucose conditions. This interaction was validated by coimmunoprecipitation analyses (Fig. 1b), and cell fractionation revealed that high glucose-induced the translocation of approximately 20% of cytosolic ADSL to the ER (Supplementary Fig. 1b), indicating the redistribution of ADSL and its interaction with INSIG1/2 on the ER in response to high glucose. To determine the underlying mechanism, we pretreated Huh7 cells with U0126, MK-2206, SU6656, and AEB071, which inhibited glucose-induced activation of ERK, AKT, c-SRC, and PKC activation, respectively (Supplementary Fig. 1c). The PKC inhibitor AEB071, but not the other inhibitors, effectively blocked the glucose-induced ER translocation of ADSL (Supplementary Fig. 1d) and its binding to INSIG1/2 (Fig. 1c).

The protein kinase C (PKC) family comprises Ser/Thr kinases present in various cell types, significantly impacting diverse signal transduction pathways[23]. This family includes at least ten members categorized into classical PKCs (α, β, γ), novel PKCs (δ, ε, η, θ), and atypical PKCs (ζ, ι/λ)[24]. AEB071 is a pan-PKC inhibitor that targets PKCα, PKCβ, PKCε, PKCδ, and PKCθ. Depletion of these PKC family members with shRNAs showed that only PKCε depletion reduced the accumulation of ADSL in the ER (Supplementary Fig. 1e). In line with previous reports[25,26], high glucose not only dramatically increased intracellular DAG levels (Supplementary Fig. 1f), but also activate PKCε in a time-dependent manner, as reflected by the membrane-distribution of PKCε and PKCε S729 phosphorylation (Supplementary Fig. 1f, g), suggesting DAG accumulation and PKCε activation occur simultaneously upon glucose stimulation. As a key activator of PKC, DAG is mainly catalyzed by phospholipase C (PLC) or Phosphatidic acid phosphatase (PAP)[27,28] (Supplementary Fig. 1h). To figure out whether DAG accumulation is required for PKCε activation in response to glucose stimulation, we treated Huh7 cells with Tolrestat (i.e., PLC inhibitor) and Propranolol (i.e., PAP inhibitor), respectively. Consistently, glucose-induced intracellular DAG accumulation (Supplementary Fig. 1i), PKCε membrane-translocation and S729 phosphorylation (Supplementary Fig. 1j) could be dramatically attenuated by Tolrestat (i.e., PLC inhibitor) and slightly abrogated by Propranolol (i.e., PAP inhibitor). These results suggested that glucose-induced PKC activation is largely dependent on PLC-mediated DAG production. Furthermore, PDHA1 (i.e., a key enzyme in glucose oxidation) depletion significantly eliminate cellular glucose oxidation (Supplementary Fig. 1k) without significantly altering glucose-induced PKCε activation (Supplementary Fig. 1l), indicating glucose oxidation plays only a limited role in PKCε activation.

Consistent results showed that reconstituted expression of the dominant-negative kinase-dead PKCε (K437R) (Supplementary Fig. 1m) inhibited high glucose-induced interactions (Fig. 1d) and colocalization (Supplementary Fig. 1n, o) between ADSL and INSIG1/2 in Huh7 cells. We performed a coimmunoprecipitation assay to determine whether PKCε binds to and phosphorylates ADSL, and showed that ADSL interacted with PKCε upon glucose stimulation in Huh7 and HCCLM3 HCC cells (Supplementary Fig. 1p). An in vitro protein phosphorylation assay, which was followed by and mass spectrometric analyses, revealed that PKCε phosphorylated ADSL at the conserved residue S407 analyses (Fig. 1e and Supplementary Fig. 2a, b). ADSL S407A mutation abolished this phosphorylation in vitro (Fig. 1e), and reconstituted expression of RNAi-resistant (r) ADSL S407A in endogenous ADSL-depleted Huh7 and HCCLM3 cells (Supplementary Fig. 2c) inhibited glucose-induced colocalization (Fig. 1f) and interactions (Fig. 1g) between ADSL and INSIG1/2. Correspondingly, an ER fractionation assay revealed that ADSL S407A was resistant to translocation to the ER upon glucose stimulation, whereas the phosphorylation-mimicking rADSL S407D mutant accumulated in the ER (Fig. 1h) even in the absence of glucose stimulation, in which assay ADSL phosphorylation was validated with a newly generated anti-ADSL pS407 antibody with confirmed specificity (Supplementary Fig. 2d–f). In addition, we constructed the Huh7 cells with knock-in expression of WT ADSL and ADSL S407A by CRISPR/Cas9 system (Supplementary Fig. 2g, h). Using these genetically engineered cell lines, we repeated the immunofluorescence and immunoblot experiments with endogenous antibodies to further confirm the co-localization and interaction of ADSL and INSIG upon glucose treatment (Supplementary Fig. 2i, j). Collectively, these results indicate that PKCε-mediated phosphorylation of ADSL at S407 is required for its ER translocation and interaction with INSIG1/2.

ER-localized ADSL activates SREBPs and promotes lipogenesis in a manner dependent on its metabolic activity

Dissociation of SCAP from INSIG1/2 facilitates the trafficking of SCAP/SREBP to the Golgi apparatus and subsequent SREBP activation[29]. As

https://doi.org/10.1038/s41467-026-70583-0

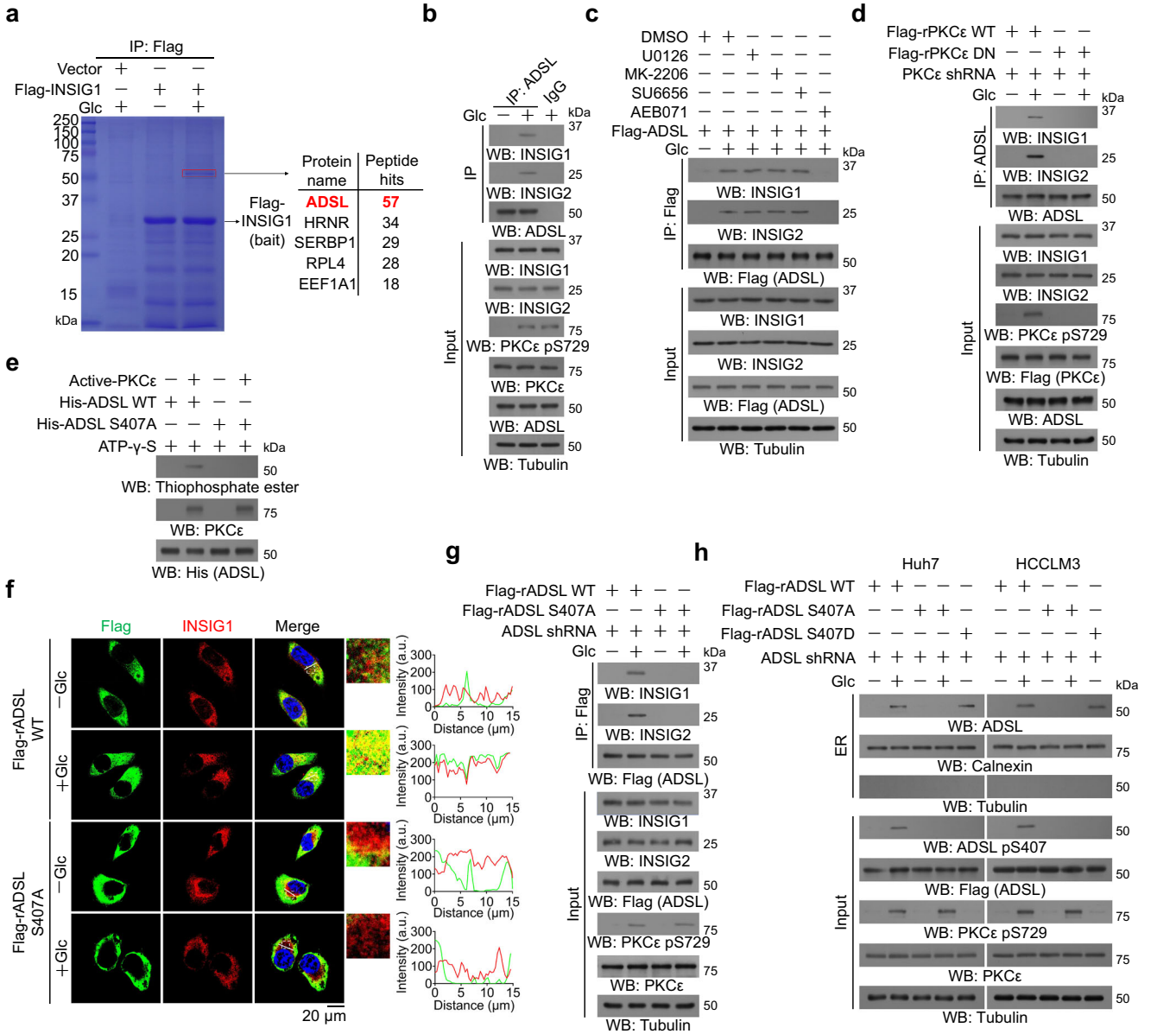

Fig. 1 | Glucose-induced and PKCε-phosphorylated ADSL binds to INSIG1/2. **a** Huh7 cells with or without expression of Flag-INSIG1 were treated with or without high glucose for 2 h. An immunoprecipitation assay was performed using anti-Flag antibody, and immunoprecipitates of Flag-INSIG1 were eluted with Flag peptide, separated using SDS-PAGE and stained with Coomassie Brilliant Blue (left). Selected peptide hits of proteins associated with Flag-INSIG1, identified through mass spectrometry, are shown (right). **b** Huh7 cells were treated with high glucose for 2 h. Immunoprecipitation and immunoblotting analyses were performed with the indicated antibodies. **c** Huh7 cells transiently transfected with Flag-ADSL were pretreated with or without U0126 (20 μM), MK-2206 (10 μM), SU6656 (4 μM), or AEB071 (5 μM) for 30 min before treatment with or without high glucose for 2 h. Immunoprecipitation and immunoblotting analyses were performed with the indicated antibodies. **d** Huh7 cells stably expressing PKCε shRNA with reconstituted expression of Flag-rPKCε WT or DN mutant protein were treated with or without high glucose for 2 h. Immunoprecipitation and immunoblotting analyses were performed with the indicated antibodies. **e** Bacterially purified His-ADSL WT or S407A protein was incubated with or without active PKCε in the presence of ATP-γ-S for an in vitro kinase assay. Immunoblotting analyses were performed with the indicated antibodies. **f** Huh7 cells stably expressing ADSL shRNA with reconstituted expression of Flag-rADSL WT or S407A mutant protein were treated with or without high glucose for 2 h. Immunofluorescence analyses were performed with the indicated antibodies. Scale bars, 20 μm. The regions in white boxes are shown at higher magnification on the right. And the intensity of green (Flag-ADSL) or red (INSIG1) fluorescent signals along the white oblique line were measured using ImageJ. **g** Huh7 cells stably expressing ADSL shRNA with reconstituted expression of Flag-rADSL WT or S407A mutant protein were treated with or without high glucose for 2 h. Immunoprecipitation and immunoblotting analyses were performed with the indicated antibodies. **h** Huh7 and HCCLM3 cells stably expressing ADSL shRNA with reconstituted expression of Flag-rADSL WT, S407A, or S407D were treated with high glucose for 2 h. ER fractions and total lysates were isolated for immunoprecipitation and immunoblotting analyses.

expected, glucose stimulation induced the dissociation of SCAP from INSIG1/2 (Fig. 2a and Supplementary Fig. 2k) and the ER (Fig. 2b), the colocalization of SCAP with the Golgi apparatus protein golgin97 (Supplementary Fig. 3a), and the cleavage (Fig. 2c), nuclear accumulation (Fig. 2d), and transcriptional activity (Fig. 2e) of SREBP-1 in Huh7 and HCCLM3 cells. Notably, this induction was attenuated by the reconstituted expression of rADSL S407A (Fig. 2a–e and Supplementary Fig. 3a), which does not obviously alter cytosolic fumarate levels (Supplementary Fig. 3b). Notably, fumarate levels within the ER fraction of ADSL S407D-reconstituted Huh7 cells were much higher than

https://doi.org/10.1038/s41467-026-70583-0

those of Huh7 cells with reconstituted expesssion of ADSL WT, S407A (i.e., S407 phosphorylation defective with cytosolic localization), A291V (i.e., catalytically inactive), S407D/A291V (i.e., S407 phosphorylation mimicking with ER localization and catalytically inactive), respectively (Supplementary Fig. 3c). The ADSL S407A mutant exhibited activity comparable to wild-type ADSL as in vitro enzyme activity assay showed (Supplementary Fig. 3d). To specify the source of substrates for INSIG-associated ADSL in the ER, we purified equal amount of ADSL protein from Huh7 cells with reconstituted expression of ADSL S407A, S407A/A291V, S407D, and S407D/A291V (Supplementary Fig. 3e), respectively. Consistently, both ADSL S407D and ADSL S407A exhibited the similar catalytic capacity to generate fumarate from both SAICAR and SAMP. As expected, catalytically inactive A291V-containing mutants (i.e., S407A/A291V and S407D/A291V) exhibited severely compromised enzymatic activity (Supplementary Fig. 3f). These results indicate that ADSL S407 phosphorylation promotes SCAP dissociation from INSIG1/2 and subsequent SREBP-1 activation, independent of cytosolic fumarate levels. Moreover, these findings demonstrate that both cytosolic ADSL and INSIG-associated ADSL in the ER utilize the same cytosolic substrates and exhibits the similar enzymatic activity.

To determine whether the metabolic activity of ADSL is involved in glucose-induced SREBP activation, we expressed rADSL A291V enzymatically inactive mutant A291V (Supplementary Fig. 3g, h), which was still phosphorylated by PKCε at S407 (Supplementary Fig. 3g) and interacted with INSIG1/2 upon glucose stimulation (Supplementary

Fig. 2 | ADSL activates SREBP pathway in an enzymatic dependent manner. **a**, **b** Huh7 cells stably expressing ADSL shRNA with reconstituted expression of the indicated ADSL protein were treated with or without high glucose. Immunoprecipitation and immunoblotting analyses were performed (**a**). The statistical analysis of INSIG1 and INSIG2 grayscale values was derived from 3 independent experiments. Immunofluorescence analyses were performed (**b**). Scale bars, 20 μm. The white arrows indicate the Calnexin-localized SCAP; The intensity of green (Calnexin) or red (SCAP) fluorescent signals along the white oblique line was measured using ImageJ. The abbreviation "a.u." stands for arbitrary units. **c**, **d** HCC cells stably expressing ADSL shRNA with reconstituted expression of the indicated ADSL protein were treated with high glucose. Immunoblotting analyses (**c**) and immunofluorescence analyses were performed with the indicated antibodies (**d**). Scale bars, 20 μm. The representative images are shown (**d**, left). The relative nucleus intensity was quantified over 30 cells by ImageJ (**d**, right). $n = 10$ microscopic fields. **e** Huh7 cells expressing ADSL shRNA with reconstituted expression of the indicated ADSL protein were subjected to a luciferase reporter assay ($n = 6$ biological replicates). **f** Huh7 and HCCLM3 cells expressing ADSL shRNA with reconstituted expression of the indicated ADSL protein were treated with high glucose. Immunoblotting analyses were performed with the indicated antibodies. **g** Huh7 cells expressing ADSL shRNA with reconstituted expression of the indicated ADSL protein were stimulated with or without high glucose. The mRNA expression levels were measured using quantitative PCR ($n = 3$ biological replicates). **h** The incorporation of ^{14}C-glucose into triglycerides (TGs) (left) and fatty acids (FAs) (right) was measured ($n = 6$ biological replicates). **i** Huh7 cells expressing ADSL shRNA with reconstituted expression of the indicated ADSL protein were stimulated with or without high glucose. Fluorescence staining were used with Bodipy and DAPI. Scale bars, 20 μm. The representative images are shown (left). The average number of lipid droplet was quantified (right). The relative nucleus intensity was quantified over 30 cells by ImageJ (right). $n = 10$ microscopic fields. All data are presented as mean ± SD. Statistical significance was determined by a two-way ANOVA (**d, e, g**, and **i**) and a one-way ANOVA (**h**).

Fig. 3i). However, ADSL A291V expression inhibited the glucose-induced disassociation of SCAP from INSIG1/2 (Supplementary Fig. 3j) and the ER (Supplementary Fig. 3k), SCAP translocation to the Golgi apparatus (Supplementary Fig. 3l), and the cleavage (Fig. 2f), nuclear accumulation (Supplementary Fig. 3m), and transcriptional activity (Supplementary Fig. 3n) of SREBP-1 in HCC cells. These results indicate that both ADSL S407 phosphorylation and ADSL metabolic activity are indispensable for the dissociation of SCAP from INSIG1/2 and SREBP-1 activation. Consistently, expression Flag-rADSL S407A and Flag-rADSL A291V decreased glucose-induced expression of mRNAs (Fig. 2g) and proteins (Supplementary Fig. 3o) of SREBP-1 targeted lipogenesis genes, including fatty acid synthase (*FASN*), acetyl-CoA carboxylase alpha (*ACACA*), stearoyl-CoA desaturase (*SCD*), and glycerol-3-phosphate acyltransferase 1 (*GPAM*). In addition, the expression of the ADSL mutants inhibited SREBP-2 cleavage (Supplementary Fig. 3p) and SREBP-2-mediated transcription of cholesterol biogenesis genes, including 3-hydroxy-3-methylglutaryl-CoA (*HMGC*) reductase (*HMGCR*), HMGC synthase 1 (*HMGCS1*), low-density lipoprotein receptor (*LDLR*), and squalene synthase (*FDFT1*) (Supplementary Fig. 3q).

Enhanced glycolysis leads to increased lipogenesis and lipid accumulation in lipid droplets (LDs)[10,13]. The expression of Flag-rADSL S407A and Flag-rADSL A291V decreased the levels of ^{14}C-glucose-derived triglycerides and fatty acids, as detected by ^{14}C-glucose tracing experiments (Fig. 2h) and reduced the total number of cellular lipid droplets (Fig. 2i) in Huh7 cells. These data indicate that ADSL S407 phosphorylation promotes SREBP1/2 activation and lipogenesis in a manner dependent on its metabolic activity.

ADSL promotes INSIG1/2 succination and the dissociation of oxysterols from INSIG1/2

We next investigated the mechanism underlying ADSL-mediated SREBP activation and examined the potential involvement of protein succination by ADSL-produced fumarate. We showed that INSIG1 (Fig. 3a) and INSIG2 (Supplementary Fig. 4a) were succinated in HCC cells upon glucose stimulation, and this effect was further enhanced by ectopic expression of HA-ADSL, which was contingent upon its expression level. In addition, supplementing Huh7 cells with dimethyl fumarate (DMF) increased INSIG1/2 succination levels in a dose-dependent manner (Supplementary Fig. 4b, c). LC-MS/MS analyses of INSIG1 immunoprecipitates revealed that INSIG1 is succinated at the evolutionarily conserved C167 residue (Supplementary Fig. 4d, e and Supplementary Data 1–3), which corresponds to the conserved C111 residue in INSIG2. The succination of INSIG1 at C167 (Fig. 3b, c) and INSIG2 at C111 (Supplementary Fig. 4f, g) in response to ADSL expression or DMF treatment was detected with a specificity-validated antibody that recognizes succinated C167 of INSIG1 and C111 of INSIG2 (Supplementary Fig. 4h–l). Following immuno-depletion experiments using an anti-INSIG1/2 scC167/C111 antibody, subsequent quantification revealed that glucose treatment induces succination in approximately 30% of INSIG1/2 proteins (Supplementary Fig. 4m). Notably, reconstituted expression of ADSL S407A or A291V mutants abolished this succination (Fig. 3d); moreover, both glucose-induced ADSL phosphorylation and INSIG1/2 succination were dramatically abrogated by the PKCε inhibitor (i.e., AEB0071), whereas the mTORC1 inhibitor (i.e., Rapamycin) exerted minimal effect on these processes (Supplementary Fig. 4n). These results strongly indicate that ADSL-mediated INSIG1/2 succination under high-glucose in a PKCε-dependent manner.

Oxysterols bind to INSIG1/2, inducing the retention of the SCAP-SREBP complex within the ER[8]. We showed that the incubation of purified His-INSIG1 (Fig. 3e) or His-INSIG2 (Supplementary Fig. 5a) with WT ADSL, but not with ADSL A291V, in the presence of the ADSL substrate SAICAR, induced INSIG1/2 succination and markedly reduced the binding of INSIG1/2 to [^{3}H]25-hydroxycholesterol. Consistently, Flag-streptavidin-binding peptide-tagged INSIG1 (Fig. 3f and Supplementary Fig. 5b) or INSIG2 (Supplementary Fig. 5c, d) exhibited a reduced ability to bind [^{3}H]25-hydroxycholesterol in Huh7 cells expressing WT ADSL, but not ADSL S407A or ADSL A291V. In addition, in the presence of fumarate, the ability of purified WT His-INSIG1 (Fig. 3g) and His-INSIG2 (Supplementary Fig. 5e), but not His-INSIG1 C167S or His-INSIG2 C111S, to bind [^{3}H]25-hydroxycholesterol decreased. Consistent with this finding, glucose stimulation decreased the binding of WT Flag/Strep-INSIG1 (Fig. 3h) and Flag/Strep-INSIG2 (Supplementary Fig. 5f), but not Flag/Strep-INSIG1 C167S or Flag/Strep-INSIG2 C111S, to [^{3}H]25-hydroxycholesterol.

We conducted molecular dynamic simulations to investigate the interaction between 25-hydroxycholesterol (i.e., 25HC) and both the WT-INSIG2-SCAP complex and the scC111-INSIG2-SCAP complex, each with separate 400 ns long-timescale simulations. Throughout the simulations, the RMSD of 25HC with WT-INSIG2-SCAP exhibited stable oscillation around 4.0 Å, indicating consistent binding. Conversely, the average RMSD of 25HC with scC111-INSIG2-SCAP showed a gradual increase in later stages, suggesting unstable binding (Fig. 3i). Analysis of the conformations throughout the simulations demonstrated a consistent binding of 25HC to the active pocket of WT-INSIG2-SCAP. However, while 25HC initially bound stably to the active pocket of scC111-INSIG2-SCAP, it gradually dissociated in later stages, suggesting an unstable binding to the active pocket of scC111-INSIG2-SCAP (Fig. 3j).

The SREBP pathway maintains cellular sterol homeostasis by integrating signals from both cholesterol and oxysterols. Oxysterols (e.g., 25-hydroxycholesterol) bind to INSIG to induce INSIG-SCAP association, while cholesterol binds to SCAP to promote SCAP-INSIG interaction. This dual-sensor system ensures precise regulation of lipogenesis[30]. To delineate the regulatory interplay between INSIG's

https://doi.org/10.1038/s41467-026-70583-0

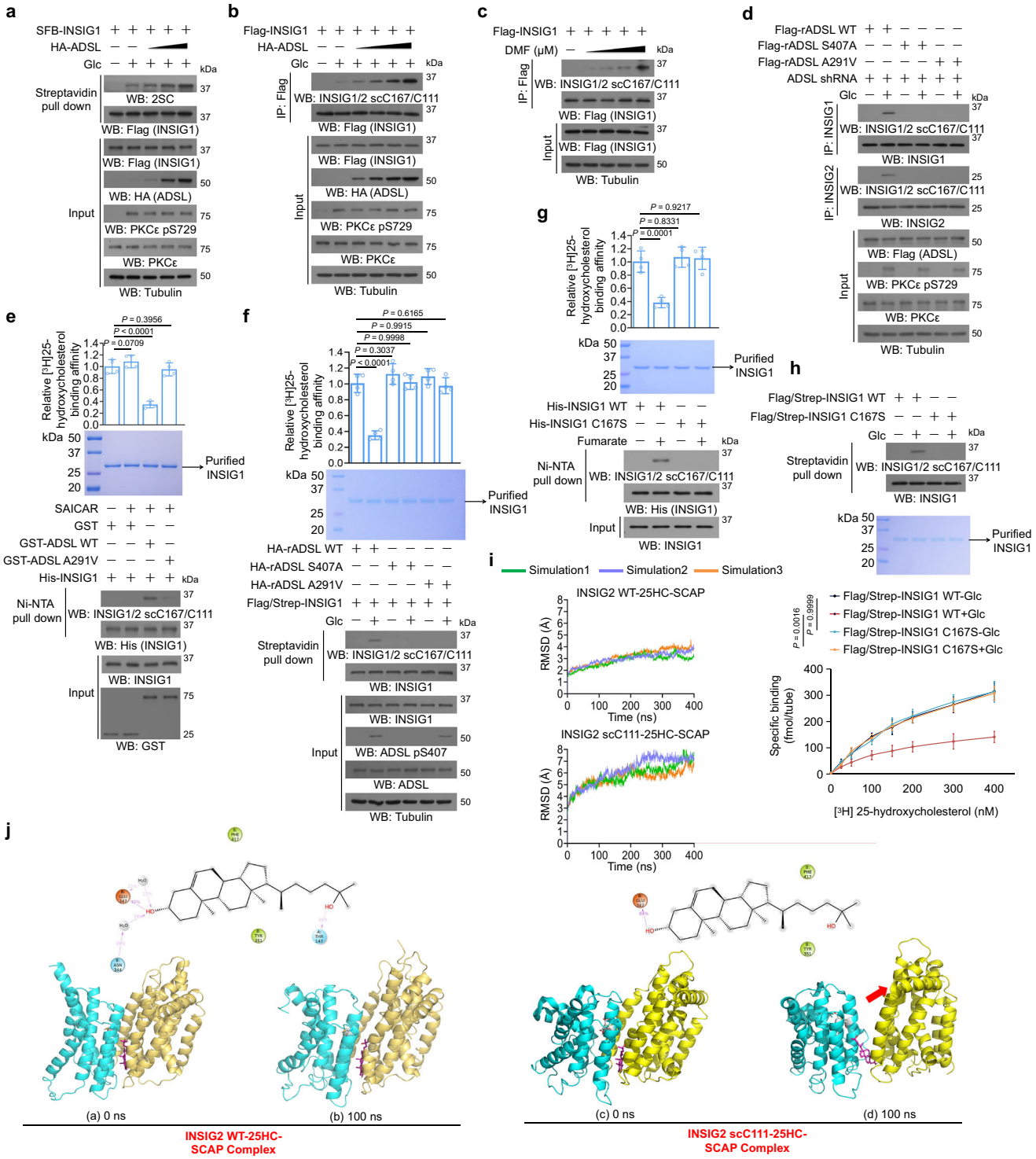

oxysterol-sensing capacity and SCAP's cholesterol-sensing capability in SREBP pathway modulation, we constructed Huh7 cell with reconstituted expression of (i) ADSL WT/ SCAP WT, (ii) ADSL S407D/SCAP WT (defective in oxysterol binding to INSIG), (iii) ADSL WT/SCAP L315F (i.e., cholesterol-sensing deficient mutant), and (iv) ADSL S407D/ SCAP L315F (defective in oxysterol binding to INSIG and cholesterol-sensing deficient), respectively. Consistently, both reconstituted expression of SCAP L315F (i.e., cholesterol-sensing deficient mutant) and ADSL S407D (i.e., defective in oxysterol binding to INSIG) could activate SREBP pathway in comparison to their WT counterpart (Supplementary Fig. 5g, h), as reflected by the impaired interaction between INSIG1/2 and SCAP (Supplementary Fig. 5g), the enhanced SREBP-1 cleavage (Supplementary Fig. 5g), and the increased SRE-driven transcriptional activity (Supplementary Fig. 5h), respectively. Of note, the aforementioned SREBP-1 activation could be boosted to a greater extend in response to combinational reconstitution of ADSL S407D/ SCAP L315F (defective in oxysterol binding to INSIG and cholesterol-sensing deficient) (Supplementary Fig. 5g, h). These data, therefore, supported that the oxysterol-sensing capacity of INSIG and the cholesterol-sensing capability of SCAP constitute a cooperative regulatory mechanism governing SREBP pathway activity. To further clarify whether ADSL-mediated SREBP activation upon glucose treatment is regulated by SCAP sterol-sensing function, we treated Huh7 cells with increasing cholesterol concentrations in the presence of high

Fig. 3 | ADSL promotes succination of INSIG1/2 C167/C111 to impair its binding affinity to oxysterols. a–d Huh7 cells transfected with the indicated plasmid were treated with or without high glucose (**a**, **b**). Huh7 cells transfected with Flag-INSIG1 were treated with increased amount of DMF for 4 h (**c**). Huh7 cells expressing ADSL shRNA with reconstituted expression of indicated ADSL protein were stimulated with or without high glucose (**d**). Total lysates were harvested for immunoprecipitation and immunoblotting analyses (**a**–**d**). **e**–**g** His-INSIG1 purified from Huh7 cells were incubated with the bacterially purified GST-ADSL WT, S407A, or A291V in the presence or absence of SAICAR (**e**). Flag/Strep-INSIG1 purified from the indicated Huh7 cells were treated with or without high glucose (**f**). His-INSIG1 WT and C167S were treated with or without fumarate (**g**). The INSIG proteins on Ni-NTA agarose beads or Streptavidin beads were washed and incubated with 400 nM [^{3}H] 25-hydroxycholesterol. Specifically bound [^{3}H]25-hydroxycholesterol was measured (**e**–**g**, upper) ($n = 4$ biological replicates). Pull down assay and immunoblotting analyses were performed (**e**–**g**, lower). **h** Flag/Strep-INISG1 WT or C167S purified from Huh7 cells were treated with or without high glucose. Streptavidin pull down and immunoblotting analyses were performed (upper). The INSIG1 proteins on Streptavidin beads were incubated with the indicated concentration of [^{3}H]25-hydroxycholesterol. Specifically bound [^{3}H]25-hydroxycholesterol was measured (lower) ($n = 3$ biological replicates). **i** Root-mean-square-deviation (RMSD) of the INSIG2-25HC-SCAP (upper) and INSIG2 scC111 -25HC-SCAP (lower) from GaMD simulations. Each color represents an independent experimental replicate. **j** Interaction profile of the INSIG2 WT-25HC-SCAP and INSIG2 scC111-25HC-SCAP complex. Different frames of binding modes of INSIG2 WT-25HC-SCAP and INSIG2 scC111-25HC-SCAP complex in 250 ns simulations. INSIG2 and SCAP are shown in cyan and orange, respectively. The red arrow indicates that INSIG2 scC111 moved away from SCAP during the simulation. 25HC is shown in purple; Residues color such as green, violet, and blue represent hydrophobic, positive charged, and polar residue, respectively. Images (lower) were prepared using PyMOL. PDB code: 6M49. All data are presented as mean ± SD. Statistical significance was determined by a two-way ANOVA (**e**–**h**).

glucose (Supplementary Fig. 5i–l). Consistently, high glucose- or ADSL S407D-mediated SREBP-1 activation could not be abrogated until excessive addition of cholesterol (150 nM), which is ~tenfold higher than cholesterol physiological concentration (15–30 nM), as reflected by the enhanced interaction between INSIG1/2 and SCAP (Supplementary Fig. 5i, k), the decreased SREBP-1 cleavage (Supplementary Fig. 5i, k), and the impaired SRE-driven transcriptional activity (Supplementary Fig. 5j, l), respectively. As expected, the aforementioned inhibitory effect of supraphysiological cholesterol (150 nM) on glucose-mediated SREBP activation could be eliminated upon reconstituted expression of SCAP L315F (i.e., sterol-sensing defective mutant). Mechanistically, this data illustrated that the regulatory effect of SREBP results from the combinational inputs from SCAP's sterol-sensing function and INSIG's oxysterol-sensing capacity, which could be dramatically attenuated by ADSL S407 phosphorylation upon glucose stimulation.

ADSL-mediated INSIG1/2 succination promotes SREBP activation

The release of oxysterols from INSIG1/2 activates SREBP[5]. As expected, knock-in expression of INSIG1 C167S/INSIG2 C111S (Supplementary Fig. 6a–d) attenuated glucose-induced the disassociation of SCAP from INSIG1/2 (Fig. 4a) and the ER (Fig. 4b); SCAP translocation to the Golgi apparatus (Supplementary Fig. 6e); the cleavage (Fig. 4c), nuclear accumulation (Fig. 4d), and transcriptional activity (Fig. 4e) of SREBP-1; and the mRNA (Fig. 4f) and protein (Supplementary Fig. 6f) expression of SREBP-1 target genes, including *FASN*, *ACACA*, *SCD*, and *GPAM*, in HCC cells. The expression of these mutants also inhibited SREBP-2-mediated transcription of genes, including *HMGCR*, *HMGCS1*, *LDLR*, and *FDFT1* (Supplementary Fig. 6g); decreased ^{14}C-glucose-derived triglyceride and fatty acid production (Fig. 4g); and reduced the total number of cellular lipid droplets (Fig. 4h) in HCC cells. To investigate the binding between succinated INSIG proteins and SCAP, we performed a pull-down assay (Supplementary Fig. 6h). Consistently, excessive addition of fumarate could trigger INSIG succination and subsequent INSIG-SCAP complex disruption, which is similar to INSIG1 W210A (i.e., a well-established SCAP-binding deficient mutant)[5]. In contrast, INSIG C167S mutant could eliminate the aforementioned fumarate-induced INSIG succination and its dissociation with SCAP. Crucially, INSIG1 C167S/INSIG2 C111S knock-in cells abolished ADSL S407D-induced SREBP-1 cleavage (Supplementary Fig. 6i). Streptavidin pull-down assay further revealed that high glucose could promote INSIG1/2 succination and attenuate the binding of INSIG to 25HC in parental Huh7 cells expressing WT INSIG1/2 but not INSIG1/2 2C/S mutant (Supplementary Fig. 6j). These data demonstrated that ADSL-mediated INSIG1/2 succination decreases its binding affinity to 25HC and promotes SREBP-1 activation upon high glucose stimulation.

To establish the functional significance of ADSL-mediated succination in regulating INSIG-SREBP pathway, we employed ADSL S407A and S407D mutants alongside DMF rescue experiments. The results found that reconstituted expression of ADSL S407D not only promotes INSIG1/2 C167/C111 succination, but also dramatically activates SREBP pathway, as reflected by the enhanced disruption of SCAP-INSIG complex (Supplementary Fig. 7a), the increased Golgi-translocation of SCAP (Supplementary Fig. 7b, c), and the elevated expression of SREBP-1 downstream target genes (Supplementary Fig. 7d) in comparison to ADSL S407A counterpart. Notably, the aforementioned impaired INSIG1/2 C167/C111 succination and SREBP pathway upon ADSL S407A reconstitution could be rescued by dimethylfumarate (DMF) in a dose-dependent manner. These data further supported the role of ADSL S407 phosphorylation and subsequent INSIG1/2 C167/C111 succination in glucose-mediated SREBP activation in the HCC cell line. Notably, DMF supplementation rescued [^{3}H]25-hydroxycholesterol dissociation from INSIG1/2 (Supplementary Fig. 7e, f) and SREBP-1 cleavage (Supplementary Fig. 7g) in S407A- and A291V-expressing Huh7 cells confirming that ADSL-derived fumarate orchestrates SREBP pathway regulation through succination-dependent remodeling of INSIG protein.

To further validate the regulatory effect of INSIG1/2 C167D/C111D on glucose-induced SREBP activation, we generated Huh7 cells with knock-in expression of INSIG1/2 C167D/C111D using the CRISPR/Cas9 system (Supplementary Fig. 7h, i). Surprisingly, INSIG1/2 C167D/C111D expression partially induced SCAP-INSIG dissociation, SREBP nuclear translocation, and SREBP-mediated gene expression in the absence of high glucose stimulation, suggesting that INSIG1/2 C167D/C111D mutants exhibited a similar SREBP-promoting effect with INSIG1/2 C167/C111 succination (Supplementary Fig. 7j–l). To this end, we compared the molecular characteristics of C-succination and aspartic acid (D) residue and observed their structural similarities (Supplementary Fig. 7m), which disrupted the SCAP-INSIG complex formation, as reflected by molecular dynamics (MD) simulation (Supplementary Fig. 7n). Taken together, these data further supported that glucose-mediated INSIG-SCAP dissociation and subsequent SREBP activation are largely dependent on INSIG1/2 C167/C111 succination in HCC cells.

Sequential activation of ADSL-INSIG-SREBP circuitry fuels HCC-specific metabolic rewiring

Dose-response experiments showed that increasing glucose concentrations (1.25 mM to 100 mM) enhanced PKCε S729 phosphorylation, ADSL S407 phosphorylation, INSIG1/2 succination, and SREBP-1 cleavage (Supplementary Fig. 8a). To further validate the aforementioned sequential cascade of ADSL-INSIG-SREBP axis, we treated Huh7 cells with high glucose for different time points, respectively (i.e., 0, 1, 2, 6, 8, 12, 24, 36 h). Consistently, high glucose treatment rapidly

https://doi.org/10.1038/s41467-026-70583-0

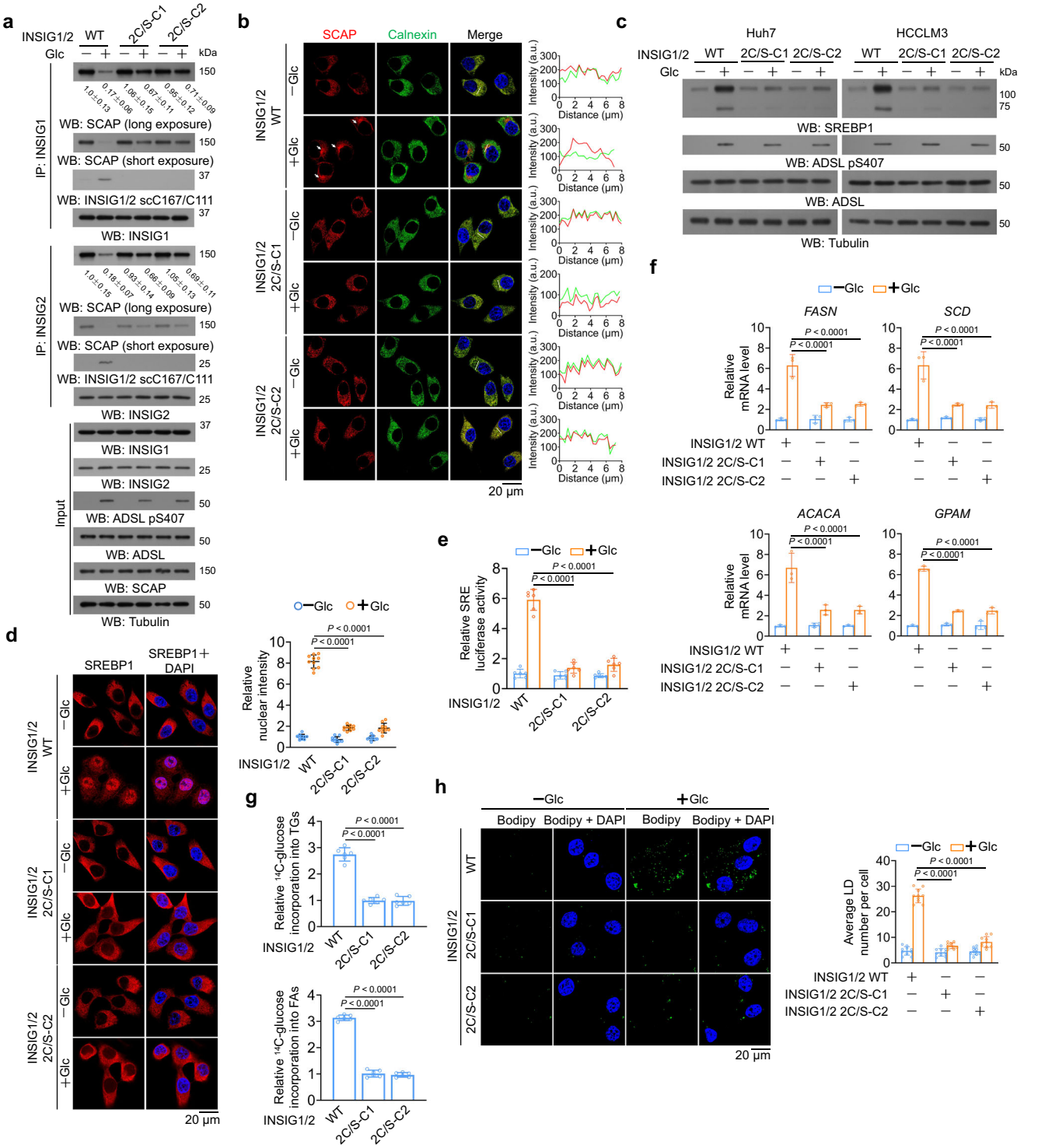

induces the robust phosphorylation of PKCε and ADSL within 2 h, followed by a significant increase in INSIG1/2 succination (i.e., peaks occur at 2 ~ 6 h post-treatment) (Supplementary Fig. 8b), dissociation of SCAP from INSIG1/2 (i.e., peaks occur at 6 ~ 8 h post-treatment), and cleavage of SREBP-1 (i.e., peaks occur at ~12 h post-treatment). These data, therefore, suggested that high glucose-induced ADSL S407 phosphorylation, INSIG1/2 succination, and subsequent SREBP-1 cleavage occur in a time- and dose-dependent manner.

To explore the sequential relationship between INSIG1/2 succination-mediated INSIG-25HC dissociation and INSIG-SCAP dissociation in response to high glucose stimulation, we constructed Huh7 cell with reconstituted expression of WT SCAP and SCAP D428A mutant (i.e., defective in the dissociation from INSIG[31]), respectively (Supplementary Fig. 8c). Consistently, both glucose-induced INSIG-SCAP dissociation and SREBP-1 cleavage could be dramatically attenuated by SCAP D428A reconstitution (Supplementary Fig. 8c). Nevertheless, reconstituted expression of SCAP D428A could not alter glucose-induced phosphorylation of ADSL S407, succination of INSIG1/2, and dissociation of INSIG1 to 25HC in comparison to its WT counterpart (Supplementary Fig. 8c). These data not only suggested that ADSL-mediated INSIG1/2 succination activates SREBP-1 in a manner dependent on the dissociation of INSIG from SCAP upon glucose stimulation, but also illustrated that INSIG1/2 succination-mediated INSIG-25HC dissociation occurs prior to INSIG-SCAP dissociation.

Fig. 4 | ADSL mediated succination of INSIG1/2 promotes SREBP activation. **a** Parental Huh7 cells and the indicated clones with knock-in expression of INSIG1 C167S/INSIG2 C111S were stimulated with or without high glucose for 4 h. Total lysates were harvested for immunoprecipitation and immunoblotting analyses. The statistical analysis of SCAP grayscale values was derived from 3 independent experiments. **b** Parental Huh7 cells and the indicated clones with knock-in expression of INSIG1 C167S/INSIG2 C111S were stimulated with or without glucose for 4 h. Immunofluorescence analyses were performed. Scale bars, 20 μm. The white arrows indicate the Calnexin-localized SCAP. The intensity of red (SCAP) or green (Calnexin) fluorescent signals along the white oblique line was measured using ImageJ. **c**, **d** Parental Huh7 and HCCLM3 cells as well as the indicated clones with knock-in expression of INSIG1 C167S/INSIG2 C111S were treated with glucose for 8 h. Total lysates were harvested for immunoblotting analyses as indicated (**c**). Immunofluorescence analyses were performed with the indicated antibodies (**d**). Scale bars, 20 μm. The representative images are shown (left). The relative nucleus intensity was quantified over 30 cells by ImageJ (right). $n = 10$ microscopic fields. **e** Parental Huh7 cells and the indicated clones of Huh7 cells with knock-in expression of INSIG1 C167S/INSIG2 C111S were subjected to a luciferase reporter assay. The relative SRE luciferase activity after normalization to β-galactosidase activity is shown ($n = 6$ biological replicates). **f** The mRNA expression levels of SREBP-1 target genes were measured using quantitative PCR ($n = 3$ biological replicates). **g** The incorporation of 14C-glucose into TGs (upper) and FAs (lower) was measured ($n = 6$ biological replicates). **h** Parental Huh7 and HCCLM3 cells as well as the indicated clones with knock-in expression of INSIG1 C167S/INSIG2 C111S were treated with glucose. Fluorescence staining was used with the Bodipy and DAPI. Scale bars, 20 μm. The representative images are shown (left). The average number of lipid droplets was quantified by ImageJ (right). $n = 10$ microscopic fields. All data are presented as mean ± SD. Statistical significance was determined by a two-way ANOVA (**d**–**f**, **h**) and one-way ANOVA (**g**).

Taken together, we concluded that high glucose in tumor cells induces ADSL-mediated INSIG1/2 succination, which impairs its binding to 25HC. The decreased binding affinity of INSIG1/2 to 25HC leads to SCAP/SREBP dissociation from INSIG1/2, triggering the translocation of SCAP/SREBP complex from ER to the Golgi apparatus, where SREBP-1 is sequentially cleaved by S1P and S2P, releasing SREBP-1 N-terminal fragment into the nucleus to activate downstream target genes transcription. These aforementioned molecular events occur sequentially (Supplementary Fig. 8d).

To confirm whether the sequence of molecular events for SREBP-1 activation is observed in non-tumoral cells, we have conducted experiments in primary human hepatocytes (PHH) and normal liver cell lines (i.e., THLE-2). As expected, high glucose treatment substantially activated ADSL-INSIG-SREBP axis in HCC cell lines (i.e., Huh7 and HCCLM3), as reflected by the dramatic increase in ADSL S407 phosphorylation, INSIG1/2 C167/C111 succination and subsequent SREBP-1 activation (Supplementary Fig. 9a). However, the aforementioned glucose-mediated effects were considerably attenuated in primary Human Hepatocyte (PHH) and normal liver cell line THLE-2 (Supplementary Fig. 9a), suggesting that the activation of ADSL-INSIG-SREBP axis in HCC cells is much more robust than that of normal cells or hepatocytes upon glucose treatment. To investigate whether the ADSL-INSIG-SREBP axis is a global effect in normal liver cells, we next expressed ADSL S407A in endogenous ADSL-depleted normal liver cell lines HL7702 and THLE-2 (Supplementary Fig. 9b). Of note, the glucose-induced increases in ADSL S407 phosphorylation, INSIG1/2 C167/C111 succination, SREBP-1 cleavage (Supplementary Fig. 9c), transcriptional activity (Supplementary Fig. 9d), and the mRNA expression of SREBP-1 target genes (Supplementary Fig. 9e) were largely impaired upon reconstituted expression of S407A, supporting that ADSL-INSIG-SREBP axis exists in normal liver cells.

To further explore whether other mechanisms, such as transcriptional regulation or protein degradation, involved in ADSL-mediated SREBP activation. We evaluated mRNA levels of *SREBF1* (encoding SREBP-1) and monitored key glucose-responsive events in Huh7 cells with endogenous SCAP knockdown reconstituted with WT SCAP or the SCAP D428A mutant (i.e., defective in the dissociation from INSIG). Consistently, high glucose markedly induced *SREBF1* transcription, ADSL S407 phosphorylation, and INSIG1/2 C167/C111 succination, which collectively promoted SREBP-1 proteolytic activation. Notably, in SCAP D428A-expressing cells, while the aforementioned glucose-mediated effects were completely abolished (Supplementary Fig. 9f–i). To further confirm whether the positive regulatory effects of ADSL-INSIG axis on SREBP-1 is cause by the enhanced protein stability of SREBP, cycloheximide (CHX) chase assays and found that reconstitution of ADSL S407 (i.e., S407 phosphorylation defective mutant), A291V (i.e., enzymatically inactive mutant), or INSIG1/2 2C/S (i.e., succination deficient munat) exhibited the comparable SREBP-1 degradation rates in comparison to their WT counterparts (Supplementary Fig. 9j–m). These data, together with the main findings in our manuscript, supported ADSL-mediated SREBP-1 activation is largely dependent on INSIG1/2 succination and subsequent dissociation of INSIG from SCAP upon glucose stimulation.

Collectively, these findings demonstrate that the ADSL-INSIG-SREBP axis functions as an evolutionarily conserved glucose-sensing cascade in both HCC and normal hepatocytes, operating sequentially through a mechanism independent of transcriptional regulation or protein degradation.

The HIV NNRTI Elsulfavirine inhibits SREBP activation by blocking the ADSL-INSIG1/2 interaction

To further analyze the ADSL-INSIG1/2 interaction, we constructed ADSL and INSIG1/2 truncation mutants (Fig. 5a, b) and showed that ADSL domain2 (Fig. 5c and Supplementary Fig. 10a) and C-termini of INSIG1 (Fig. 5d) and INSIG2 (Supplementary Fig. 10b) are required for their binding. Subsequent molecular docking analyses revealed three potential interaction models (Supplementary Fig. 10c). Mutations of the potential interacting residues showed that mutations of Phe208, Val324, Trp326, and Phe327 in ADSL (Fig. 5e) and of Leu210 and Tyr213 in INSIG2 (Fig. 5f) diminished the interaction between ADSL and INSIG2. Consistently, both AlphaFold2 (Supplementary Fig. 10d) and Chai-1 (Supplementary Fig. 10e) successfully reproduced this structural model3. Based on these results, the structural interaction between ADSL and INSIG2 was further defined (Fig. 5g, h), and the stability of the model was further supported by the RMSD (Fig. 5i) and RMSF (Fig. 5j) values.

By simulating the amino acid residues involved in the interaction of ADSL with INSIG2 (Fig. 5k) and performing pharmacophore-based and docking-based virtual screens of the FDA-approved drug library for identification of the drugs that bind to the interacting interface of the ADSL-INSIG2 complex, three drugs with superior docking scores were selected (Fig. 5l). Treatment of HCC cells with these three drugs showed that only Elsulfavirine, a nonnucleoside reverse transcriptase inhibitor (NNRTI) that has been used for the HIV treatment, effectively blocked the binding of ADSL to INSIG2 in vitro (Fig. 5m) and glucose-induced the interaction between ADSL and INSIG1/2 in Huh7 cells (Fig. 5n), as well as the accumulation of ADSL in the ER (Supplementary Fig. 10f).

To evaluate the impact of Elsulfavirine to the ADSL-INSIG2 complex, we conducted molecular dynamics (MD) simulation and showed that Elsulfavirine interacted with INSIG2 (Fig. 6a, b) and increased the instability of the complex (Fig. 6c), with ADSL moving further away from INSIG2 over the course of 0–200 ns (Fig. 6d). We further examined the binding of VM1500A, the active metabolite derived from Elsulfavirine hydrolysis. Molecular dynamics simulations indicated that the hydrolyzed acetyl group does not contribute additional protein interactions, and the overall binding conformation aligns closely with that of both protonation states of the parent prodrug

https://doi.org/10.1038/s41467-026-70583-0

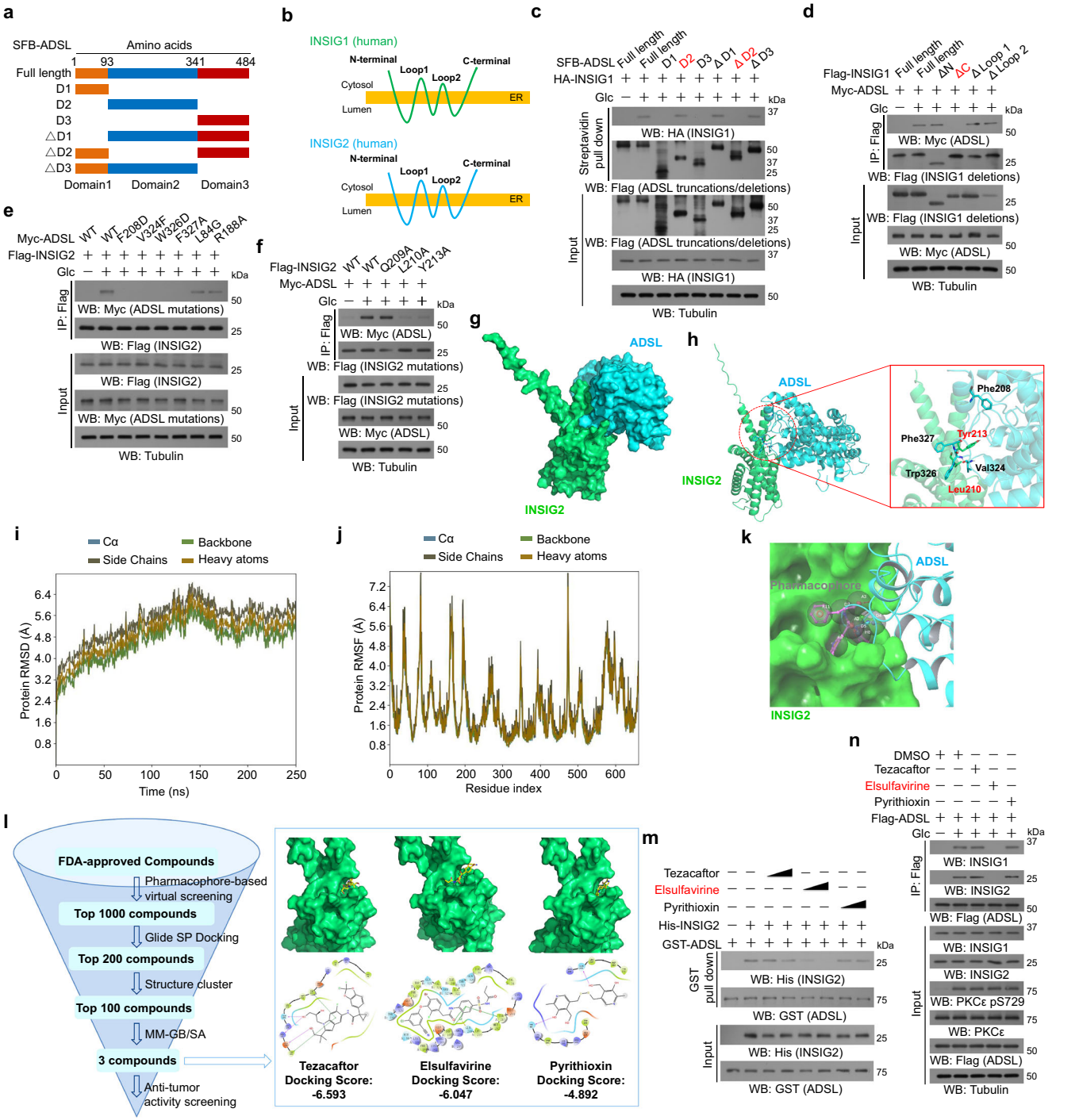

Fig. 5 | The HIV NNRTI Elsulfavirine blocks the ADSL-INSIG1/2 interaction. **a** Schematics of the full-length ADSL and truncation constructs. **b** The topological structures of INSIG1 and INSIG2, which have 59% amino acid sequence identity. **c**–**f** Huh7 cells transfected with the indicated plasmids were treated with or without high glucose. Total lysates were harvested for immunoprecipitation and immunoblotting analyses. **g** The binding complex of INSIG2-ADSL complex was built based on the protein-protein complex (INSIG2 AlphaFoldDB: Q9Y5U4, ADSL PDB code: 4FLC). The protein is presented in surface representation; INSIG2 and ADSL are shown in green and cyan, respectively. **h** The conformation of the INSIG2-ADSL complex (left); detailed interaction of INSIG2 with ADSL and key residues (right). The protein is presented in cartoon and sticks representation; INSIG2 and ADSL are shown in green and cyan, respectively. **i** RMSD of the α-C atom, backbone, side chains, and Heavy atoms of the protein. **j** The Root Mean Square Fluctuation of the protein reflects local changes along the protein chain. **k** The pharmacophore model of key residues Val324, Trp326, and Phe327. Pharmacophoric features were shown as bubble (hydrogen bond acceptor, red; hydrogen bond donor, blue; hydrophobic, cyan; hydrophobic-aromatic ring, orange) Residues color are shown as pink. **l** Schematic workflow of the pharmacophore-based and docking-based virtual screening for small-molecule inhibitors of INSIG2-ADSL inhibitors (left); binding mode and interaction profile of the top 3 inhibitors complex with INSIG2-ADSL (right). H-bond, Metal coordination, and salt bridge are shown in yellow, purple, and red color, respectively. Residues color such as green, violet, and blue represent hydrophobic, positive charged, and polar residue, respectively. **m** A GST pulldown assay was performed by mixing purified His-INSIG2 with purified GST-ADSL, followed by incubation with or without Tezacaftor (5 μM, 50 μM), Elsulfavirine (2 μM, 25 μM), or Pyrithioxin (10 μM, 100 μM) for 1 h. Immunoblotting analyses were performed as indicated. **n** Huh7 cells with Flag-ADSL transfection were pretreated with or without Tezacaftor (20 μM), Elsulfavirine (10 μM), Pyrithioxin (100 μM) for 1 h before treatment with or without high glucose for 12 h. Immunoprecipitation and immunoblotting analyses were performed with the indicated antibodies.

https://doi.org/10.1038/s41467-026-70583-0

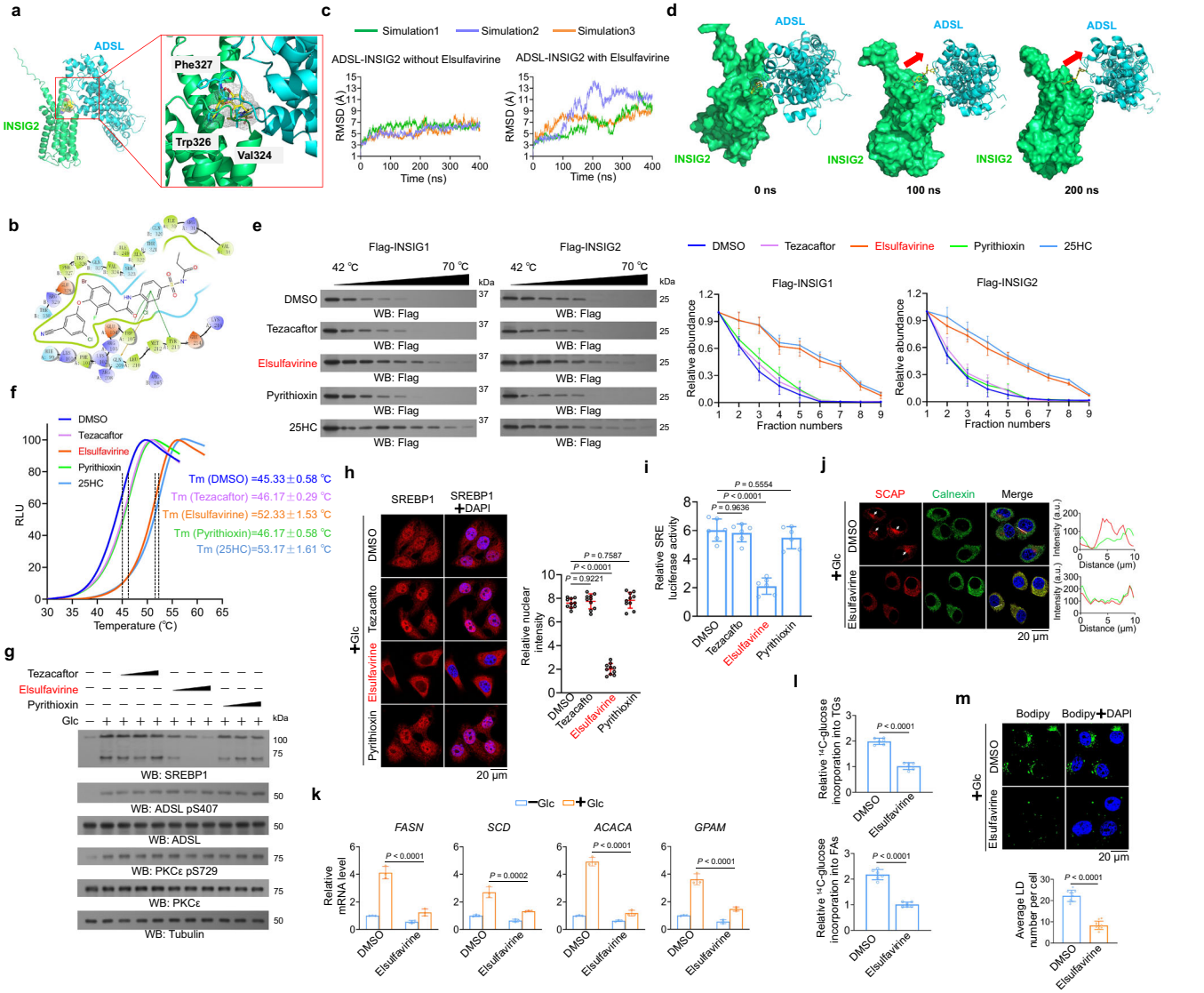

Fig. 6 | Elsulfavirine block SREBP-1 activation through impair ADSL-INSIG1/2 binding upon glucose stimulation. a The binding complex of INSIG2-Elsulfavirine-ADSL complex was built based on the protein-protein model. **b** Interaction profile of the INSIG2-Elsulfavirine-ADSL. Residues color such as green, violet, and blue represent hydrophobic, positive charged, and polar residue, respectively. **c** RMSD of the INSIG2-ADSL in the absence (left) or presence (right) of compound Elsulfavirine from GaMD simulations. **d** Different frames of binding modes of INSIG2-Elsulfavirine-ADSL complex in 250 ns simulations. **e** Target engagement assay using Flag-INSIG1 or Flag-INSIG2 purified from Huh7 cells treated with or without indicated drugs (left). The relative distribution of each protein in different fractions was quantified by densitometric analysis of the blots ($n = 3$ biological replicates) (right), Data are mean ± SD. **f** The interaction of INSIG2 with Elsulfavirine detected by thermal shift assay. RLU, relative light units. The data were shown as the relative mean values of RLU ($n = 3$ biological replicates). **g**, **h** Huh7 cells were pretreated with or without Tezacaftor, Elsulfavirine, or Pyrithioxin for 1 h before treatment with or without high glucose. Immunoblotting analyses were performed (**g**). Immunofluorescence analyses were performed (**h**, left). Scale bars, 20 μm. The relative nucleus intensity was quantified over 30 cells by ImageJ (**h**, right). $n = 10$ microscopic fields. **i** Huh7 cells were treated with or without Tezacaftor, Elsulfavirine, or Pyrithioxin for 1 h and then subjected to a luciferase reporter assay ($n = 6$ biological replicates). **j**, **k** Huh7 cells treated with Elsulfavirine were stimulated with or without high glucose. Immunofluorescence analyses were performed (**j**). Scale bars, 20 μm. The mRNA expression levels of SREBP-1 target genes were measured using quantitative PCR (**k**) ($n = 3$ biological replicates). **l** The incorporation of ^{14}C-glucose into TGs (upper) and FAs (lower) was measured ($n = 6$ biological replicates). **m** Huh7 cells were pretreated with or without Elsulfavirine in high glucose for 12 h. Fluorescence staining were used with the Bodipy and DAPI (upper). Scale bars, 20 μm. The average number of lipid droplets was quantified by ImageJ (lower). $n = 10$ microscopic fields. All data are presented as mean ± SD. Statistical significance was determined by a one-way ANOVA (**h, i**), two-way ANOVA (**k**), or two-tailed *t*-test (**l**, **m**).

(Supplementary Fig. 10g, h). Molecular docking analyses showed that Elsulfavirine, docked within the pocket of the ADSL-INSIG2 complex, exhibits numerous interactions with INSIG2 (Supplementary Fig. 10i, j). In addition, the target engagement assay and thermal shift assay also showed that Elsulfavirine, rather than tezacaftor or pyrithioxin, interacted with INSIG1/2 with kinetics comparable to 25-hydroxycholesterol (Fig. 6e, f).

In line with these findings, treatment of HCC cells with Elsulfavirine could effectively blocked the glucose-induced SREBP-1 cleavage (Fig. 6g), nuclear accumulation of SREBP-1 (Fig. 6h), and SRE transcriptional activity (Fig. 6i). Elsulfavirine also inhibited the glucose stimulation-induced colocalization of ADSL-INSIG (Supplementary Fig. 10k), disassociation of SCAP from the ER (Fig. 6j), translocation of SCAP to the Golgi apparatus (Supplementary Fig. 10l), mRNA (Fig. 6k)

and protein (Supplementary Fig. 10m) expression of SREBP-1 target genes, synthesis of ^{14}C-glucose-derived triglycerides and fatty acids (Fig. 6l), and lipid droplet accumulation (Fig. 6m) in HCC cells. Taken together, these findings indicate that Elsulfavirine efficiently inhibits SREBP activation by disrupting the interaction between ADSL and INSIG1/2.

ADSL-mediated SREBP activation promotes HCC progression

SREBP activation promotes tumor cell proliferation[32]. As expected, reconstituted expression of ADSL S407A and ADSL A291V or knock-in expression of INSIG1 C167S/INSIG2 C111S in HCC cells inhibited HCC cell proliferation (Supplementary Fig. 11a, b). Consistently, mouse studies showed that the expression of these mutants in Huh7 cells, which were intrahepatically (Fig. 7a, b) or subcutaneously (Supplementary Fig. 11c–f) injected into athymic nude mice, markedly inhibited tumor growth, which accompanied by decreased Ki-67 expression (Supplementary Fig. 11g, h) and increased cell apoptosis in tumors (Supplementary Fig. 11i, j). In addition, ADSL S407A expression decreased the succination of INSIG1 at C167 and INSIG2 at C111 and reduced the expression and nuclear accumulation of SREBP-1 (Fig. 7c). Similarly, INSIG1 C167S/INSIG2 C111S expression also decreased the nuclear level of SREBP-1 (Fig. 7d). These results indicate that ADSL-mediated INSIG1 succination and SREBP activation promote liver tumor growth.

Additionally, we employed hydrodynamics-based transfection in mice to administer plasmids for the expression of active myr-AKT, c-Met, and the Sleeping Beauty transposase (which induces rapid liver tumour growth)[32,33] along with either wild-type ADSL, ADSL S407A, or ADSL A291V, respectively. Notably, expression of the ADSL mutants (S407A and A291V) significantly suppressed tumor growth (Supplementary Fig. 11k, l), accompanied by reduced INSIG1/2 succination and attenuated of SREBP-1 expression (Supplementary Fig. 11m). Consistently, the inhibitory effects of succination-deficient INSIG1/2 mutants (C167S/C111S) on tumor growth (Supplementary Fig. 11n, o) and tumoral SREBP-1 expression (Supplementary Fig. 11p) were also validated by the aforementioned Sleeping Beauty (SB) transposon system. These data further supported the pro-tumorigenic role of ADSL-INSIG-SREBP axis in HCC.

We injected luciferase-expressing Huh7 cells expressing WT INSIG1/2 and INSIG1/2 2C/S mutant orthotopically into the liver of nude mice, respectively. Consistently, knock-in expression of INSIG1/2 2C/S mutant significantly suppressed tumor growth (Supplementary Fig. 11q, r), accompanied by impaired INSIG1/2 succination and attenuated SREBP-1 expression (Supplementary Fig. 11s). Consistently, the aforementioned inhibitory effects of succination-deficient INSIG1/2 mutants (C167S/C111S) on tumor growth (Supplementary Fig. 11q, r) and tumoral SREBP-1 expression (Supplementary Fig. 11s) were largely eliminated by 2-deoxy-D-glucose (2-DG) (i.e., glucose analog that mimics glucose deprivation). These data further supported the critical role of glucose-dependent succination in SREBP activation and tumor growth.

To assess the clinical implications of ADSL-mediated SREBP activation, we conducted immunohistochemistry (IHC) analyses on 30 paired samples of primary HCC and adjacent normal tissues. The phosphorylation of ADSL at S407 and succination of INSIG1 at C167/INSIG2 at C111, as well as the nuclear expression of SREBP-1, were significantly increased in HCC specimens compared to normal tissues (Supplementary Fig. 12a). Moreover, these markers were strongly correlated with each other in 84 resected HCC tumors (Supplementary Fig. 12b). Importantly, elevated levels of ADSL S407 phosphorylation and INSIG1 C167/INSIG2 C111 succination, as well as increased nuclear SREBP-1 expression in HCC samples, were associated with reduced overall survival durations in patients with HCC (Fig. 7e, f). These findings support the finding that the ADSL-mediated succination of INSIG1/2 plays a crucial role in the clinical aggressiveness of human HCC.

To investigate the therapeutic potential of Elsulfavirine in HCC treatment, we evaluated the effects of Elsulfavirine alone and in combination with the first-line liver cancer chemotherapy lenvatinib. Elsulfavirine and lenvatinib each alone inhibited tumor growth (Fig. 7g, h), along with decreased Ki-67 expression (Supplementary Fig. 12c), increased cell apoptosis in tumor tissues (Supplementary Fig. 12d), and reduced SREBP-1 expression and the levels of lipid synthesis-related enzymes, such as FASN and ACLY, in the tumor tissue (Fig. 7i). Notably, an additive effect was observed for the combined treatment with the two drugs. These pivotal in vivo findings were further corroborated in luciferase-expressing Hepa1-6 tumor-bearing animal models (Supplementary Fig. 12e–i). Collectively, our results propose a promising combinatorial strategy targeting both proliferative and metabolic vulnerabilities in HCC, highlighting the translational potential of Elsulfavirine-lenvatinib synergy.

Discussion

Metabolic alterations are a key hallmark of cancer cells, and increased lipid biosynthesis is a critical and universal metabolic dependency of cancer cells across different cancer types[34,35]. The Warburg effect fuels lipid biosynthesis[36,37]. We demonstrated that glucose stimulation activated PKCε in hepatocellular carcinoma cells, leading to the phosphorylation of ADSL at S407 and the ER translocation. In the ER, phosphorylated ADSL bound to INSIG1/2, and ADSL-produced fumarate promoted the succination of INSIG1 at C167 and INSIG2 at C111. This succination decreased the binding affinity of oxysterols for INSIG1 and INSIG2 and disrupted the interaction of INSIG1/2 with SCAP. Consequently, the SCAP-SREBP complex translocated to the Golgi apparatus, where it promoted SREBP1/2 activation, the transcription of downstream genes required for de novo lipogenesis, tumor cell proliferation, and tumorigenesis. In addition, the phosphorylation of ADSL at S407, the succination of INSIG1 at C167, and the succination of INSIG2 at C111 were not only positively associated with the nuclear accumulation of SREBP-1 in human HCC specimens but also correlated with poor disease prognosis (Fig. 7j). These findings unveil a mechanism by which tumor cells sense glucose levels and convey a moonlighting function of ADSL in enhancing lipogenesis for tumor growth.

Fumarate governs various metabolic and cellular pathways to drive tumor progression[38,39], yet the mechanism by which fumarate fine-tunes lipid synthesis remains largely elusive. Metabolic enzymes have the potential to interact with diverse proteins, assuming non-canonical roles through the localized formation of metabolic byproducts and thereby influencing the activities of intricate proteins[36,40,41]. The binding of ADSL to INSIG1/2 likely augments the availability of fumarate locally, facilitating INSIG1/2 succination and triggering SREBP activation by diminishing the binding between INSIG1/2 and oxysterols. These findings underscore the meticulous control of lipogenesis by integrated metabolite-dependent regulation of key transactional protein complexes, as reflected by the release of the metabolite oxysterol from INSIG1/2 regulated by the metabolite fumarate.

Modulation of protein–protein interactions is an approach to intervene in the function of untargetable transcription factors. Through structure-based screening, Elsulfavirine, a clinically used HIV NNRTI, disrupted the ADSL-INSIG1/2 complex and markedly inhibited SREBP activation. The efficient inhibition of tumor growth by the combined therapy of Elsulfavirine with lenvatinib represents a readily available approach with the potential to improve therapy for difficult-to-treat HCC.

Methods

This work complies with all relevant ethical regulations. Animal studies were approved by the Research Ethics Committee and complied with the ethical regulations of Experimental Animal Ethics Committee of The First Affiliated Hospital, Zhejiang University School of Medicine.

https://doi.org/10.1038/s41467-026-70583-0

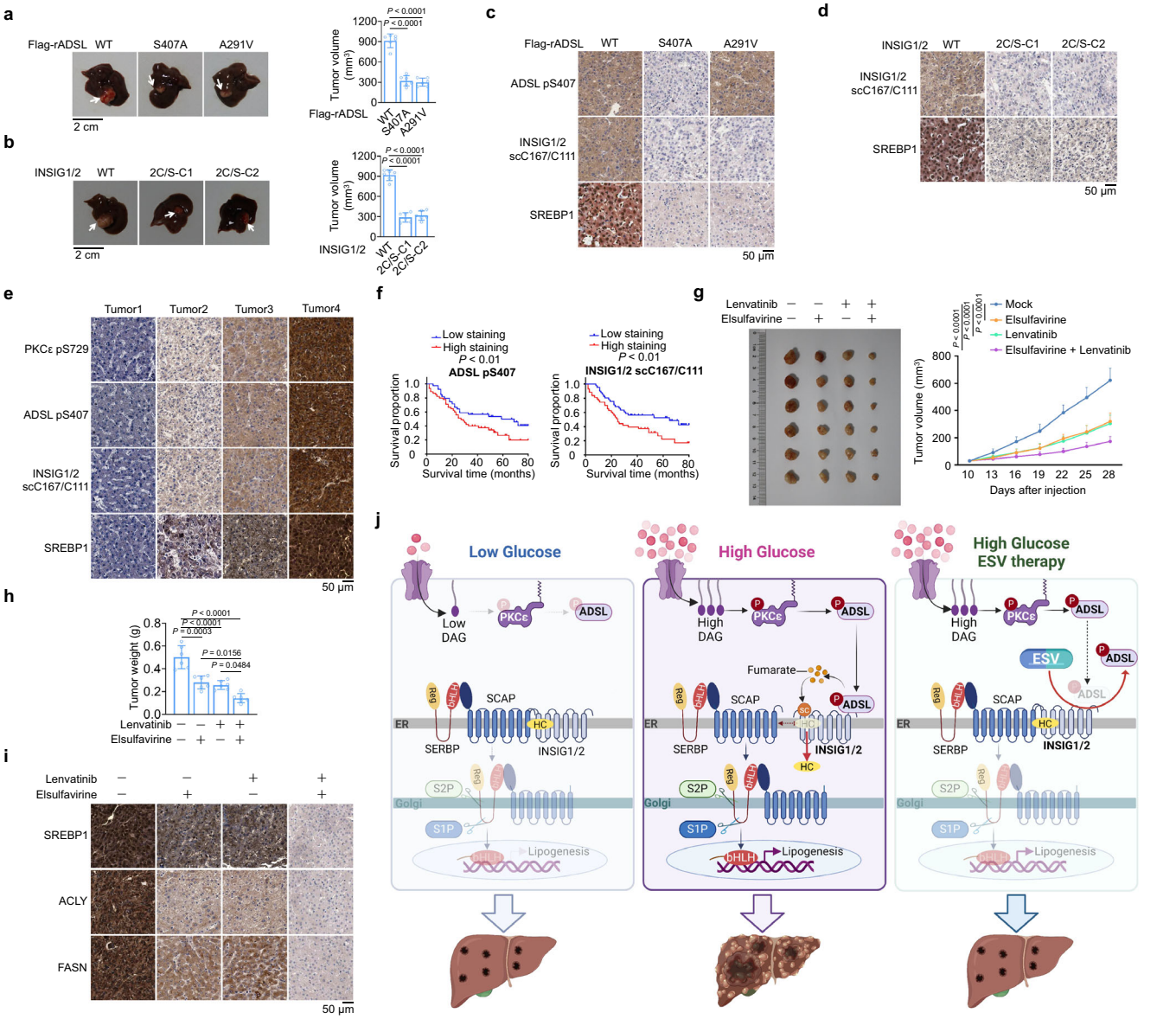

Fig. 7 | ADSL-INSIG-SREBP axis promotes HCC progression. a Huh7 cells expressing ADSL shRNA with reconstituted expression of the indicated ADSL proteins were injected into athymic nude mice ($n = 6$ mice/group). Tumor growth was examined 28 days after injection. The arrows indicate tumors. Tumor volumes were calculated (right). **b** Parental Huh7 cells and the indicated clones of Huh7 cells with knock-in expression of INSIG1 C167S/INSIG2 C111S were injected into athymic nude mice ($n = 6$ mice/group). Tumor growth was examined 28 days after injection. The arrows indicate tumors. Tumor volumes were calculated (right). **c**–**e** IHC analyses of the indicated tumors ($n = 6$) were performed with the indicated antibodies. Representative staining images are shown. Scale bars, 50 μm. **f** Kaplan–Meier plots of the overall survival rates in 84 patients with HCC grouped according to high (staining score, 4–8) and low (staining score, 0–3) expression of ADSL pS407 (ADSL pS407 high, $n = 45$; low, $n = 39$) or INSIG1/2 C167/C111 succination (INSIG1/2 succination high, $n = 43$; low, $n = 41$). *P* values were calculated using a log-rank test (two-tailed). **g**, **h** Tumor growth of Huh7 cells in athymic nude mice treated with control, Elsulfavirine, Lenvatinib, or the combination ($n = 6$ mice/group). On the 7th day after inoculation, the mice were intraperitoneally injected with drugs every day. The mice were euthanized and examined for tumor growth 28 days after injection. Tumor volumes were calculated (**g**). Tumor weights were calculated (**h**). **i** IHC analyses of the indicated xenograft tumors ($n = 6$) were performed with the indicated antibodies. Representative staining images are shown. **j** Mechanism for ADSL-promoted activation of SREBP and lipogenesis. HC hydroxycholesterol, bHLH basic helix-loop-helix protein, Reg regulatory domain of SREBP. This figure was created using BioRender (Hu, Z. (2025) https://BioRender.com/t3u0tg1). All data are presented as mean ± SD. Statistical significance was determined by a one-way ANOVA (**a**, **b**) or two-way ANOVA (**g**, **h**).

The use of human HCC samples and the relevant database was approved by the Research Ethics Committee of the Second Affiliated Hospital, Zhejiang University School of Medicine.

Materials

Rabbit antibodies against ADSL (ab154872), INSIG1(ab70784), PKCε S729 (ab63387), SRC (pY418) (ab4816), Calnexin (ab22595), Ki-67 (ab21700), SREBP-1 (ab28481), SREBP-2 (ab28482), SCAP (ab125186), SCD1 (ab19862), ATP1A1 (ab7671) and FASN (ab22759) were purchased from Abcam (Cambridge, United Kingdom). Antibodies against PKCε (#2683), AKT (#9272), Phospho-p44/42 MAPK (Erk1/2) (Thr202/Tyr204) (#9106), AKT (pS473) (#4060), c-SRC (#2108), HA-tag (#50297) (mouse), HA-tag (#3724) (rabbit), PLCγ1 pY783 (#2821) were purchased from Cell Signaling Technology (Danvers, MA), Rabbit antibodies against PKCα (A0267), PKCβ (A21241), PKCδ (A7778), PLCγ1 (A7711) were purchased from ABclonal (WuHan, China). Normal mouse IgG (sc-2025), normal rabbit IgG (sc-2027), mouse ADSL (sc-365623), PKCθ (sc-81534), ERK1/2 (sc-514302), SREBP-1 (sc-13551), His (sc-8036),

GST (sc-138), and tubulin (sc-8035) antibodies were obtained from Santa Cruz Biotechnology. ATP-γ-S (ab138911) and Diacylglycerol assay kit (ab242293) were obtained from Abcam. 2SC (crb2005017) was purchased from Cambridge Research Biochemicals. [^{3}H]25-hydroxycholesterol was obtained from PerkinElmer. U0126, MK-2206, SU6656, AEB071, SAICAR, Elsulfavirine, Tezacaftor, and Pyrithioxin were purchased from MedChemExpress. Lenvatinib was purchased from Selleck Chemicals. Streptavidin magnetic beads, anti-Flag M2 agarose beads, EDTA-free protease inhibitor cocktail, fumarate, 3 × Flag peptides, Recombinant active PKCε (14–518), fumarate assay kit (MAK060), mouse anti-Flag (F1804), rabbit anti-Flag (F7425) antibodies, and cholesterol (C8667) were purchased from Sigma-Aldrich (St. Louis, MO). Hygromycin (400053), puromycin (540222), and G418 (345810) were purchased from EMD Biosciences (San Diego, CA). INSIG2 (PA5-41707), Golgin97 (CDF4) (14-9767-82), BODIPY(D3922), Calnexin (MA3-027), glutathione agarose, 4′, 6-diamidino-2-phenylindole (DAPI), Alexa Fluor 488 goat anti-rabbit (A11008), Alexa Fluor 594 goat anti-rabbit (A11012), Alexa Fluor 488 goat anti-mouse (A11029), and Alexa Fluor 594 goat anti-mouse antibodies (A11005) were obtained from Thermo Fisher Scientific. Tolrestat (HY-16500), Propranolol (HY-B0573B), Ramapycin (HY-10219), and 2-deoxy-D-glucose (HY-13966) were purchased from MedChemExpress. PDH E1 Alpha (18068-1-AP) and ACLY (15421-1-AP) Polyclonal antibodies were purchased from Proteintech. Secondary HRP-coupled antibodies were used at 1:5000. Ni-NTA agarose was obtained from Qiagen. ADSL pS407 and INSIG1/2 scC167/C111-specific antibodies were generated by ABclonal Biotechnology. The antibody applications and dilution ratios are detailed in the reporting summary.

DNA construction and mutagenesis

PCR-amplified human ADSL, PKCε, INSIG1, INSIG2, and SCAP were cloned into pcDNA3.1/hygro(+)-(Flag, HA, or twin Flag/Streptavidin), pCDH-CMV-MCS-EF1-Puro/Neo-(Flag, HA), CS2MT (7-Myc), PGEX4T-1 (GST), pColdI (His) or pT3-EF1a vector. His-tagged INSIG1 and INSIG2 were constructed in a pFastBac Dual expression vector as previously described[42]. pT3-EF1a-c-Met was a gift from X. Chen (Addgene plasmid 31784). The following mutations were generated using a QuikChange site-directed mutagenesis kit (Stratagene, La Jolla, CA): ADSL S407A, S407D, A291V, F208D, V324F, W326D, F327A, L84G, R188A, INSIG1 C167S, F171A, W210A, INSIG2 C111S, Q209A, L210A, Y213A, PKCε K437R and SCAP L315F, D428A, as well as short hairpin RNA (shRNA)-resistant ADSL (human) constructs containing A465G, T468C, C471T and A474G, shRNA-resistant ADSL (mouse) constructs containing T366C, T369C and G372T, shRNA-resistant PKCε constructs containing A2058G, A2061C and C2065A, shRNA-resistant SCAP constructs containing C3078T, T3081C, C3084A and C3087A. The PLKO.1 shRNA target sequences were as follows: PRKCA, 5′- CGAGGTGAAGGACCACAAATT -3′, PRKCB, 5′- CCTGTCAGATCCCTACGTAAA -3′, PRKCQ, 5′-CAAGGCCGAATGCTAATGAAT -3′, PRKCD, 5′- CAGAGCCTGTTGGGATATATC -3′, PRKCE, 5′- CCACAAGTTCGGTATCCACAA -3′, ADSL (human), 5′- GCAGAACATTTCTGAAGGATT -3′, ADSL (mouse), 5′-CCTGCTATGTCGGAGACAATA -3′, SCAP, 5′′- GCTCAACGGTTCCCTTGATTT -3′, PDHA1-shRNA1: 5′- GCCAATCAGTGGATCAAGTTT -3′, PDHA1-shRNA2: 5′-CGAATGGAGTTGAAAGCAGAT -3′.

Cell culture and transfection

Huh7, HCCLM3, and 293T cells were procured from ATCC. These cell lines were cultured in complete Dulbecco's modified Eagle's medium (DMEM) supplemented with 10% dialyzed bovine calf serum (HyClone). Notably, none of the cell lines employed in our study were listed in the database of commonly misidentified cell lines maintained by the International Cell Line Authentication Committee and NCBI Biosample. Transfections were performed using Lipo8000™ Transfection Reagent (Beyotime) according to manufacturer instructions. Cells were seeded in 60-mm dishes at 4×10^5 cells/dish 18 h before transfection. For each transfection: 2 μg plasmid was diluted in 150 μL serum-free medium, separately mixed with 3.2 μL Lipo8000™ diluted in 150 μL serum-free medium. The mixture was gently mixed by pipetting (no incubation required) and added dropwise to cell cultures. For generating shRNA-depleted stable cell lines, cells were transfected with shRNA plasmids targeting ADSL or PKCε, and selected by puromycin. For generating gene-expressing stable cell lines, shRNA-depleted cells were transfected with lentivirus carrying shRNA-resistant (r) WT rADSL, rADSL S407A, rADSL A291V, WT rPKCε, or rPKCε K437R (DN), and selected by hygromycin. Before high-glucose (25 mM) treatment, the cells were cultured in low-glucose (1.25 mM) medium for 16 h. U0126 (20 μM), MK-2206 (10 μM), SU6656 (4 μM) or AEB071 (5 μM) was added 30 min before treatment with or without high-glucose.

Purification of recombinant proteins

His-ADSL WT, S407A, and A291V were bacterially expressed and purified as described previously[32]. Flag/strep-tagged INSIG1/2 in Huh7 cells were isolated using anti-Flag agarose beads and eluted with 3 × Flag peptides. Subsequently, after ultrafiltration and removal of the 3 × Flag peptides, a secondary streptavidin pull-down was conducted. His-INSIG1 and His-INSIG2 were purified as previously described[43].

In vitro kinase assay

The in vitro kinase assays were conducted following established protocols[32,44]. In brief, Active PKCε (14–518, Sigma-Aldrich) at 500 ng was co-incubated with bacterially purified His-ADSL (200 ng) in a kinase buffer (25 mM Tris-HCl [pH 7.5], 5 mM beta-glycerophosphate, 2 mM dithiothreitol [DTT], 0.1 mM Na_3VO_4, and 10 mM $MgCl_2$) along with 50 mM ATP-γ-S at 30 °C for 30 min. Following incubation, samples were alkylated with 50 mM PNBM/5% DMSO, incubated at room temperature for 1 h, and subsequently subjected to analysis via SDS-PAGE and immunoblotting. Phosphorylated proteins were visualized using an anti-thiophosphate ester antibody sourced from Abcam (ab92570).

CRISPR-Cas9-mediated genome editing

Genomic mutations in INSIG1(C167S) and INSIG2(C111S) were induced in cells using the CRISPR-Cas9 system, following established methods[45,46]. Custom-designed single-guide RNAs (sgRNAs) targeting regions adjacent to the mutation sites were integrated into a PX458 vector (Addgene) after BbsI restriction enzyme digestion. Huh7 and HCCLM3 Cells, initially seeded at 60% confluency, were then co-transfected with sgRNAs (0.5 μg) and single-stranded donor oligonucleotides (10 pmol) to facilitate mutation introduction. After 24 h, cells were trypsinized, single cells were isolated, and seeded into 96-well plates. Genomic DNA was then extracted from GFP-positive cells, and PCR products spanning the mutation sites were sequenced. sgRNA targeting sequence for INSIG1 (C167S): 5′-CGCTGCATAGCAGTTTTTGT-3′; single-stranded donor oligonucleotide (ssODN) sequence for INSIG1 (C167S): 5′-TACTGTACCCCTGTATCGACAGTCACCTCGGAGAACCCCACAAATTTAAGAGAGAATGGGCCAGTGTCATGCGCTcCATcGCcGTcTTTGTTGGCATTAACCACGCCAGTGCTGTATCCTTAATTTTCTGTGCTACGTCCAGAGTATCTTCTTAGGTTATATAT-3′. sgRNA targeting sequence for INSIG2 (C111S): 5′-CGGTGTGTAGCAGTCTTTGT-3′; ssODN sequence for INSIG2 (C111S): 5′- GTTATTATACCCCTGCATTGACAGACATCTAGGAGAACCACATAAATTTAAAAGAGAGTGGTCCAGTGTAATGCGGTcTGTcGCcGTaTTTGTTGGTATAAATCATGCCAGTGCTGTATCCTTTACTCTGTAATGAAATGCATAATAACAAAGTGGCTTCCAAC-3′; sgRNA targeting sequence for ADSL (S407A): 5′-AATCAGAGTGCTTCTCAGC-3′; ssODN sequence for ADSL (S407A): 5′-ACGCCCTGTTAGTAGGGAACTGACAATACTTCACTGTCTTCCCAGGATTGCCATGAGAAAATCAGAGTGCTTgCTCAGCAaGCAGCTTCTGTGGTTAAGCAGGAAGGGGGTGACAATGACCTCATAGAGCGTATCCAGGTTGATGCCTACTTCAGTCCCATTCACTCCCAGTTGGATCATTTACTGGAT-3′. The lowercase letters in the ssODN sequences

denote the mutated nucleotides intended to substitute the native nucleotides in the genomic DNA of parental cells via the CRISPR-Cas9 system. Genotyping was conducted through sequencing PCR products amplified using the following primers: INSIG1 forward: 5′-CCCTGCTTGATTCCTTCCTGT-3′, INSIG1 reverse: 5′-CCATCACTGAGTCAAAAACTTAACC-3′; INSIG2 forward: 5′-CCTCATTTCATTTCCTTTGGAAGGT-3′, INISG2 reverse: 5′-AGCACCTGAAGCTACCACAT-3′; ADSL forward: 5′-TCATGGCCACAGAGAACATC-3′, ADSL reverse: 5′-CTGCTGGGAGGCACGACCAG-3′.

Specific antibodies generation and validation

ADSL pS407 and INSIG1/2 scC167/C111-specific antibodies were generated by ABclonal Biotechnology. For the generation of rabbit polyclonal antibodies specific to ADSL phosphorylated at S407 and to INSIG1/2 succinated at C167/C111, the phosphopeptide IRVL-(S-phosphorylation)-QQAA-C and the succination-mimic peptide SV-Nle-R(C-Succination)IAV were synthesized. These modified peptides were conjugated to keyhole limpet hemocyanin (KLH) to serve as immunogens. Corresponding control peptides, IRVLSQQAA-C and SV-Nle-RCIAV, were also synthesized for subsequent antibody purification and detection. Four specific pathogen-free Japanese White rabbits were immunized. The immunogen IRVL-(p-S)-QQAA-C, dissolved in 8 M urea-PBS buffer, was thiol-coupled to KLH. The primary immunization administered 700 μg of immunogen per rabbit emulsified with an equal volume of complete Freund's adjuvant (CFA) via multiple subcutaneous injections in the abdominal and dorsal regions. Booster immunizations were performed at 7, 14, 21, and 21 days post-primary immunization (for a total of five immunizations), each administering 350 μg of immunogen per rabbit emulsified with incomplete Freund's adjuvant (IFA) via multiple subcutaneous injections. Serum collected one week after the fifth immunization was evaluated by dot blotting (DB), revealing detectable antibody titers at a 10,000-fold dilution of serum against the modified peptide. Rabbits were sacrificed 73 days after the initial immunization. Terminal serum was collected via carotid artery, allowed to clot overnight at 4 °C, incubated at 37 °C for 2–3 h, and clarified by centrifugation (5 min, 4 °C, 4500 × *g*). Antibodies were affinity-purified from the pooled sera using columns prepared with either the modified peptide or the control peptide. Briefly, serum was diluted tenfold in PBS, filtered through a 0.22 μm membrane, and incubated with peptide-coupled resin for 2 h. The resin slurry was then loaded onto a 1 mL column. After washing the resin four times with PBS, bound antibodies were eluted using pH 3.0 citrate buffer. The eluate (designated as the antibody fraction) was dialyzed against PBS (pH 7.3), and the antibody concentration was determined using a Nanodrop spectrophotometer. Huh7 cells were stimulated with or without high glucose, and total lysates were harvested for competition assays. For detection of ADSL S407 phosphorylation, 1 μg/mL anti-ADSL pS407 antibody was preincubated with 200 μg/mL ADSL pS395 peptide, ADSL pS407 peptide, ADSL pS412 peptide, or unmodified ADSL control peptide prior to immunoblotting. For INSIG succination detection, 1 μg/mL anti-INSIG1/2 scC167/C111 antibody was preincubated with 200 μg/mL INSIG1 scC146 peptide, INSIG1 scC167 peptide, or unmodified INSIG1 control peptide to assess INSIG1 C167 succination; the same antibody was preincubated with 200 μg/mL INSIG2 scC90 peptide, INSIG2 scC111 peptide, or unmodified INSIG2 control peptide for INSIG2 C111 succination analysis. Peptides were synthesized by Nanjing Yuanpeptide Biotechnology, with sequences as follows: ADSL pS407 peptide: HEKIRVL(p-S)QQAA, ADSL pS395 peptide: KAGG(p-S)RQDCHEKIRV, ADSL pS412 peptide: RVLSQQAA(p-S)VVKQEG, ADSL unmodified peptide: HEKIRVLSQQAA, INSIG1 scC167 peptide: SVMR(sc-C)IAVFV, INSIG1 scC146 peptide: GLLYP(sc-C)IDSHL, INSIG1 unmodified peptide: SVMRCIAVFV, INSIG2 scC111 peptide: SVMR(sc-C)VAVFV, INSIG2 scC90 peptide: GLLYP(sc-C)IDRHL, INSIG2 unmodified peptide: SVMRCVAVFV.

Glucose oxidation assay

Stable PDHA1-knockdown cell lines were generated using lentiviral-based shRNA vectors targeting PDHA1, followed by puromycin selection. For glucose oxidation assays, control and PDHA1-depleted Huh7 cells were first incubated in serum-free medium containing 2.8 mM [U-^{14}C]-glucose (0.25 μCi, representing a low-glucose condition) for 12 h, and then exposed to serum-free medium with 22.4 mM [U-^{14}C]-glucose (2 μCi, representing a high-glucose condition) for 4 h. The reaction was terminated by injecting 70% perchloric acid into the medium, and the ^{14}C-labeled CO_2 generated from glucose oxidation was captured on NaOH-soaked Whatman filter papers and quantified by scintillation counting.

Quantitative RT-PCR

Cellular RNA was isolated using TRIzol following the manufacturer's instructions (Invitrogen). In brief, 1 μg of RNA per sample underwent cDNA synthesis employing a TaqMan Reverse Transcription Reagents kit (Applied Biosystems). Quantitative real-time PCR was conducted on the LightCycler® 480 PCR system (Bio-Rad) using the SYBR Premix Ex Taq kit for Real-Time PCR (Takara). α-Tublin was utilized as the reference gene for normalization in the experiments. The following primers were used for qRT-PCR: *FASN*, 5′-CACAGGGACAACC TGGAGTT-3′ and 5′-ACTCCACAGGTGGGAACAAG-3′; *SCD*, 5′-CGAC GTGGCTT TTTCTTCTC-3′ and 5′-CCTTCTCTTTGACAGCTGGG-3′; *ACACA*, 5′-AGTGGGTCACCCCATTGTT-3′ and 5′- TTCTAACAGGA GCTGGAGCC-3′; *GPAM*, 5′-TTGTGGCTTGCCTGCTCCTCTA-3′ and 5′-AATCACGAG CCAGGACTTCCTC-3′; *HMGCR*, 5′-TCTGGCAGTCAGTGG GAACTATT-3′ and 5′-CCTCGTCCTTCGATCCAATTT-3′; *HMGCS1*, 5′-GATGTG GGAATTGTTGCCCTT-3′ and 5′-ATTGTCTCTGTTCCAACTT CCAG-3′; *LDLR*, 5′-AACGGTCATTCACCCAGGTC-3′ and 5′-GGCTGAA-GAATAGGAGTTGCC-3′; *FDFT1*, 5′-CGATAGCTGTGTGCAAAGTAACT-3′ and 5′-CCATCTGCTGAGTGCTTTCTG-3′; *α-Tubulin*, 5′- TATCGAGC GCCCAACCTACAC-3′ and 5′- CACCAGGTTGGTCTGGAATTCTGT-3′.

[^{3}H]25-hydroxycholesterol binding assay

[^{3}H]25-hydroxycholesterol binding assays were conducted following established procedures[42]. In brief, each reaction was carried out in a 100 μL final volume of buffer A (50 mM Tris-HCl at pH 7.5, 150 mM NaCl, 1 mM dithiothreitol, 0.1% Fos-choline 13, 0.005% sodium azide) comprising 1.2 μg of purified wild-type or mutant His-INSIG1 or INSIG2, 10–500 nM [^{3}H]25-hydroxycholesterol, and 25 mM phosphocholine chloride. Following a 4-h incubation at room temperature, the mixture was passed through a column packed with 0.3 mL of Ni-NTA agarose beads (Qiagen). Subsequently, each column underwent three washes with 10 mL of buffer B (50 mM Tris-HCl at pH 7.5, 150 mM NaCl, 1 mM dithiothreitol, and 0.1% (w/v) Anapoe-C12E9). The protein-bound [^{3}H]25-hydroxycholesterol was eluted using 250 mM imidazole and quantified via scintillation counting.

Luciferase reporter assay

The SRE luciferase activity in cell lysates was evaluated with the luciferase assay system. Huh7 cells were transfected in 24-well plates with 0.1 μg of SRE-driven luciferase reporter and 0.075 μg of β-galactosidase. After a 24-h transfection, the cells were subjected to high-glucose conditions. Cell lysates were then assessed for luciferase and β-galactosidase activity according to the manufacturer's guidelines (Promega).

ER fractionation

The Endoplasmic Reticulum Isolation Kit (ER0100, Sigma-Aldrich) was employed for the isolation of ER fractions from the cells.

Mass spectrometry analysis

For identification of interacting proteins, a protein band visualized via Coomassie blue staining was excised from an SDS-PAGE gel and

digested in gel in 50 mM ammonium bicarbonate buffer containing RapiGest (Waters Corporation) overnight at 37 °C with 200 ng of modified sequencing grade trypsin (Promega). The digested protein samples were analyzed using high-sensitivity LC-MS/MS with an Orbitrap Elite mass spectrometer (Thermo Fisher Scientific). Proteins were identified by searching the fragment spectra against the UniProt protein database (EMBL-EBI) using the Mascot search engine (v.2.3; Matrix Science) with the Proteome Discoverer software program (v.1.4; Thermo Fisher Scientific). For detection of phosphorylation or succination sites, in vitro PKCε phosphorylated ADSL and immunoprecipitated Flag-INSIG1 from HCC cells upon glucose stimulation were subjected to trypsin digestion and analyzed using LC-MS/MS with the Orbitrap Elite mass spectrometer. All mass spectrometry experiments were performed with at least two biological replicates.

Immunoprecipitation and immunoblotting analysis

Proteins were extracted from cultured cells using a modified buffer, followed by immunoprecipitation and immunoblotting with specific antibodies, as previously detailed[32,47]. Briefly, cells were harvested, triple-washed with cold PBS, and then lysed in a buffer comprised of 25 mM Tris-HCl (pH 7.4), 150 mM NaCl, 1% NP-40, 5 mM EDTA, 10% glycerol, 1 mM $NaVO_3$, 50 mM NaF, and a protease inhibitor cocktail for 30 min at 4 °C. Following centrifugation at 15,000 × *g*, the supernatant was carefully transferred to a prechilled microcentrifuge tube. The protein concentration was determined using the BCA Protein Assay Kit (Pierce) following the manufacturer's instructions. Approximately 10% of the supernatant was reserved for Western analysis as input controls. The rest of the protein samples were incubated with designated antibodies overnight and then combined with protein A or protein G-agarose beads for 2 h. The immunoprecipitation beads underwent five washes with lysis buffer before immunoblotting analysis. Blots were blocked with 5% non-fat milk, followed by incubation with primary antibodies and HRP-conjugated secondary antibodies.

Ni-NTA pulldown assay

Equal amounts of His-tagged purified protein (200 ng/sample) were incubated with or without 100 ng of GST fusion proteins, along with Ni-NTA agarose beads, in a modified binding buffer (50 mM Tris-HCl, pH 7.5, 1% Triton ×-100, 150 mM NaCl, 1 mM DTT, 0.5 mM EDTA, 100 μM PMSF, 100 μM leupeptin, 1 μM aprotinin, 100 μM sodium orthovanadate, 100 μM sodium pyrophosphate, 1 mM sodium fluoride). The Ni-NTA agarose beads were washed four times with the binding buffer and subsequently analyzed by immunoblotting or [^{3}H]25-hydroxycholesterol binding assay as previously described[32].

Cytosolic fumarate level detection

Cytosolic fraction was extracted as described previously[48]. Briefly, 2×10^7 Huh7 Cells were harvested by trypsinization, pelleted at 600 × *g* for 5 min and washed twice with cold PBS. The cell pellets are placed on ice and homogenized by 10 strokes using a Thomas homogenizer with a motor-driven Teflon pestle in the 2 mL of hypotonic homogenization buffer (3.5 mM Tris-HCl, pH 7.8, 2.5 mM NaCl, 0.5 mM $MgCl_2$). After homogenization, 200 μl of hypertonic buffer (0.35 M Tris-HCl, pH 7.8, 0.25 M NaCl, 50 mM $MgCl_2$) is added to make the medium isotonic. This homogenate is centrifuged at 1200 × *g* for 3 min at 4 °C to pellet unbroken cells, debris, and nuclei. The supernatant is centrifuged again at 15,000 × *g* for 2 min at 4 °C and the supernatant is cytosolic fraction. Then Fumarate Assay Kit (MAK060; Sigma) were used for cytosolic fumarate concentration measurement.

Assay of ADSL enzymatic activity and HPLC analyses

ADSL activity was assessed as previously described[49]. In brief, Ni-NTA beads conjugated recombinant His-ADSL WT, S407A, and A291V, incubated with or without active PKCε, were incubated in the reaction buffer containing 200 μM SAICAR in 20 mM Tris pH 8.1 in a final volume of 200 μL for 30 min at 37 °C. The reaction was terminated by the addition of 50 μl ice-cold 10% (w/v) $HClO_4$ and left on ice for 10 min. The sample was than centrifuged at 11,000 × *g* at 4 °C for 5 min. The supernatant was transferred to a clean vial and neutralized with 8 μl 5 M K_2CO_3. After a further 10-min incubation on ice, the sample underwent a second centrifugation, and the supernatant was filtered through a 0.2 μm nylon filter at 11,000 × *g* at 4 °C for 1 min. The filtrate was then transferred to a fresh injection vial, with 10 μL used for subsequent HPLC analysis.

Immunofluorescence analysis

Immunofluorescence analysis was conducted following previously reported[50]. Cultured cells were fixed with 4% paraformaldehyde (PFA), permeabilized with 0.1% Triton ×-100 for 5 min, and then blocked in 3% BSA for 1 h. Subsequently, the samples were incubated overnight at 4 °C with primary antibodies targeting specific antigens. Following incubation with fluorescent-dye-conjugated secondary antibodies and DAPI, immunofluorescent images of the cells were captured and visualized using a confocal microscope (Leica TCS-SP8, Germany). Co-localization analysis was performed using ImageJ, and graphs were generated using GraphPad Prism 8.

Lipid droplet staining

Huh7 cells were plated at 10,000–20,000 cells/well in 12-well plates containing 1 mL low-glucose (1.25 mM) DMEM supplemented with 10% FBS and incubated overnight at 37 °C. After aspiration, cells were stimulated with high-glucose (25 mM) medium for 12 h. Fixation was performed by adding pre-chilled 5% formaldehyde in PBS directly to culture medium (1:1 v/v) to achieve 2.5% final concentration, followed by 15-min incubation at room temperature. Fixed cells were washed twice with PBS and stained with 500 μL/well of a solution containing 10 μg/mL BODIPY 493/503 and 1 μg/mL DAPI (diluted in PBS) for 30 min at room temperature in the dark. Following two PBS washes, fluorescent images of the cells were captured and visualized using a confocal microscope (Leica TCS-SP8, Germany). The total number of lipid droplets in each image was measured using ImageJ and normalized to the number of cells to calculate the average lipid droplets per cell.

Molecular modeling

Molecular modeling was performed using Schrödinger Software Release 2021–4. The structure of INSIG2 was derived from the AlphaFold Protein Structure Database (AlphaFoldDB: Q9Y5U4) and the ADSL was derived from the Protein Structure Database (PDB code: 4FLC). The Protein Preparation Wizard tool of Maestro was used to prepare the protein structure required for subsequent docking calculations, in which missing hydrogen atoms were added and minimized, and bond orders and disulfide bonds were calculated. The structure of the protein was minimized using the OPLS4 force field to optimize the hydrogen bonding network and converge heavy atoms to an RMSD of 0.3 Å. INSIG2 is defined as the receptor, and the ADSL is defined as the ligand. The ligand was rotated into a large number of different orientations with respect to the receptor, and each of the ligand orientations was evaluated to find the best docking score to the receptor. The top 1000 rotations are clustered using the RMSD between matching atoms in each pair of rotated structures. The structure that is taken from each cluster is the one with the most neighbors in the cluster. After docking, a refinement is performed by default on the side chains of residues within 5 Å of the interface, to minimize clashes and optimize interactions.

Molecular dynamics simulation

Molecular dynamics simulations were performed to further investigate the dynamic interactions between the INSIG2 and ADSL. The simulations were conducted by using Schrödinger version 2021–4 and

employed the Desmond module. The previously generated docking complex was employed as the starting coordinates, which was then filled into a proper box and solvated with water (TIP3P). The whole system was then added corresponding Na^+ or Cl^- to neutralize all charges of the whole system. 0.15 M NaCl was added to the system to simulate salt concentrations under physiological conditions. The whole system was relaxed with the default set, and the productive simulation was then performed for 250 ns with a temperature of 300 K and a pressure of 1 bar. The resulting trajectory was then analyzed, and the RMSD of the complex was calculated. The trajectory snapshots were recorded at 1000 ps intervals. The Simulation Interaction Diagram of Desmond was used to analyze trajectories to predict the binding pattern of ADSL and INSIG2. The most abundant binding conformations were then extracted by the Desmond Trajectory Clustering module. The membrane protein structure was retrieved from the Orientations of Proteins in Membranes (OPM) database (PDB: 6M49). Following PDB import into CHARMM-GUI, the protein was subsequently oriented and positioned within a membrane bilayer composed of a 20% Cholesterol, 50% POPC (1-palmitoyl-2-oleoyl-sn-glycero-3-phosphocholine), and 30% POPE (1-palmitoyl-2-oleoyl-sn-glycero-3-phosphoethanolamine) mixture that mimics the ER membrane. The simulations employed symmetric, neutral membranes, solvated with 0.15 M NaCl using TIP3P water at 310 K. Furthermore, the construction of force fields for specific amino acids undergoing post-translational modifications is accomplished by selecting specific modification types. Each simulation was conducted using OpenMM, with input files generated by Membrane Builder. A six-step equilibration protocol, as defined by Membrane Builder, was implemented. This included 250 ps of NVT (constant particle number, volume, and temperature) dynamics with a 1 fs timestep. Subsequently, the NPT (constant particle number, pressure, and temperature) ensemble was utilized for 125 ps with a 1 fs timestep, followed by 1.5 ns with a 2 fs timestep. During the equilibration phase, the positional and conformational force constants for lipid and water molecules were progressively reduced, reaching zero at the conclusion of the equilibration process. The production was run for GaMD simulations using Amber.

Binding free energy calculation using MM-GBSA

Molecular mechanics was used to calculate the binding free energies of the ligand combination and reference complexes. The molecular mechanics-generalized Born surface area (MM/GBSA) approach was used to determine the binding free energy of protein-ligand complexes. Because of the precision of quantum mechanical computing, the number of false-positive findings in molecular docking experiments has decreased. Interaction effects on ligand-protein stability were investigated using the Prime MM/GBSA component of the Schrödinger suite. Taking multiple snapshots of the Desmond trajectory file allowed the MM-GBSA to be calculated. Finally, "Schrödinger's thermal mmgbsa.py" (https://www.schrodinger.com) was used to calculate the anticipated binding energy's mean and standard deviation throughout the 250-ns time period. The script is written in Python.

Virtual screening

For the ligand preparation, initially, FDA-approved compounds were downloaded from the MCE database in SDF format. The "LigPrep" tool in Maestro of Schrodinger software suite was utilized for ligand preparation. During ligand preparation, the following criteria, including (i) OPLS3 force field, (ii) generation of all possible ionization states at pH 7.0 ± 2.0, (iii) desalt option, (iv) generation of tautomers for all conformers, and (v) generation of one low energy conformer per ligand was implemented. The prepared ligands were subsequently taken through a structure-based virtual screening process using Glide module of Schrodinger suite. The HTVS mode was employed for filtering the chemical entities suggested from the library of molecules, SP mode was applied for further screening, and XP mode was utilized to obtain more accurate docking scores.

Target engagement assay

Target engagement assay was performed as previously reported[51]. In brief, Huh7 cells transfected with Flag-INSIG1 or Flag-INSIG2 were treated with or without 50 μM tezacaftor, 25 μM elsulfavirine, 50 μM pyrithioxin, or 25 μM 25HC for 1 h. Cells were collected, aliquoted, and heated at 42, 45, 48, 51, 54, 58, 62, 66, and 70 °C for 3 min. Flag-INSIG1 and Flag-INSIG2 in the soluble fraction was quantified by immunoblotting analysis.

Thermal shift assay

Thermal shift assay was conducted as previously reported[52]. Briefly, 0.1 mg/ml of His-INSIG2 with or without 250 μM tezacaftor/elsulfavirine/pyrithioxin/25HC in PBS was prepared, and a 1000 dilution of SYPRO Orange dye (Invitrogen) was added. Fluorescence signals were recorded as a function of temperature using a Real-Time PCR machine (Bio-Rad CFX96) in the FRET mode with fluorescence intensity measured at Ex/Em: 450–490/560–580 nm. The temperature gradient ranged from 30 to 95 °C with a ramp rate of 0.5 °C over 15 s. Data analysis was conducted using the differential scanning fluorimetry analysis tool.

Conversion of radiolabelled glucose to triglycerides and fatty acids

The incorporation of radioactive substrates into triglycerides and fatty acids was assessed as previously described[53]. Briefly, prior to the incorporation assay, cells were subjected to low-glucose treatment (i.e., 1.25 mM D-glucose in the culture medium). Cells were washed twice with PBS and then exposed to 1 mL labelling medium (2.5% fatty-acid-free bovine serum albumin, 1% (v/v) penicillin/streptomycin, 5 mM D-glucose, 0.5 mM sodium, 2 mM sodium pyruvate, 13.8 μCi/μmol ^{14}C-glucose or 10.4 μCi/μmol ^{14}C-acetate) at 37 °C in a humidified incubator (5% CO_2) for 8 h before lipid extraction. Metabolic activities were halted by washing the cells with cold PBS, followed by cell lysis using a modified Dole's extraction mixture (80 mL isopropanol, 20 mL hexane, 2 mL 0.5 M H_2SO_4). Triglycerides were extracted with hexane, washed, and then evaporated to remove the solvent. The incorporation of ^{14}C-glucose into fatty acids and triglycerides was determined by saponifying neutral lipids with KOH-ethanol (20 mL 95% ethanol, 1 mL water, 1 mL saturated KOH) at 80 °C for 1 h, followed by hydrophobic separation with hexane. The hydrophilic fraction was evaporated and quantified using liquid scintillation counting. The incorporation data were normalized based on cell count.

Animal studies

Male athymic BALB/c nude mice (6-week-old) and C57BL/6 mice (6-week-old males) were purchased from GemPharmatech (Nanjing, China). Mice were housed under specific pathogen-free (SPF) conditions in a 14-h light/10-h dark cycle. Mice were kept at ambient temperature (21–23 °C, 50% humidity) with access to water and food ad libitum. The standard rodent diet (XTI01MY-001 for BALB/c nude mice and XTI01ZJ-009 for C57BL/6 mice) was obtained from Xietong (Yangzhou, China). One million Huh7 cells expressing ADSL shRNA with reconstituted expression of the indicated Flag-rADSL proteins or parental Huh7 cells and the indicated clones with knock-in expression of INSIG1/2 C167S/C111S (2C/S) mutants were suspended in 20 μL of DMEM with 33% Matrigel and intrahepatically injected into the livers of 6-week-old male athymic BALB/c nude mice. The injections were performed as described previously[54]. Six mice constitute a group in each experiment. The animals were euthanized 28 days after injection. For treatment, Mice were subcutaneously inoculated in the right flank with Huh7 cells (1×10^6). They were then randomly divided into four groups: control group, lenvatinib group (10 mg/kg, daily), Elsulfavirine group

(10 mg/kg, daily), and combined group (10 mg/kg Lenvatinib plus 10 mg/kg Elsulfavirine). Treatment of mice included daily gavage with 0.5% methylcellulose (control group) or lenvatinib diluted in 0.5% methylcellulose by daily gavage administration for 20 days, Elsulfavirine diluted in 0.5% methylcellulose by daily gavage administration for 20 days. After twenty-eight days post-Huh7 cells injection, the tumors were excised, fixed in 4% formaldehyde, and embedded in paraffin. Tumor volume was determined using the formula $V = 1/2a^2 b$, where V represents volume, a denotes the shortest diameter, and b indicates the longest diameter. The transgenic HCC mouse model was established by overexpression of activated AKT combined with c-Met using hydrodynamic transfection[33]. Wild-type 6-week-old FVB/N mice were subjected to hydrodynamic injection as previously described[32]. In brief, the plasmids pT3-EF1a- Flag-ADSL (wild-type, S407A or A291V mutant) (20 μg), pT3-EF1a-myr-AKT (20 μg) and pT3-EF1a-c-Met (20 μg) together with pCMV/sleeping beauty transposase (SB) (2.4 μg), in a ratio of 12.5:12.5:12.5:1.5, were diluted in 2 ml saline (0.9% NaCl), filtered through a 0.22-μm filter and injected into the lateral tail vein of the male mice in 6 s. After 14 weeks, the mice were euthanized and liver tumours were extracted. The animals were treated in accordance with relevant institutional and national guidelines and regulations. The maximum tumor burden permitted by the ethics committee is 1500 cm^3, and the tumor burden did not exceed this limit. The use of the animals was approved by the Institutional Review Board at The First Affiliated Hospital, Zhejiang University School of Medicine, Hangzhou, China (Reference number: 20241731). No specific statistical method was employed to predetermine the sample size.

TUNEL assay

Mouse tumor tissues were sliced into 5-μm sections. Apoptotic cells were quantified utilizing the DeadEnd Colorimetric TUNEL System (Promega) following the manufacturer's instructions.

IHC analysis and histological evaluation of human HCC specimens

Human HCC tissue collection and study approval were reported previously[32]. Human HCC and adjacent matched nontumor tissue samples were sourced from The Second Affiliated Hospital, Zhejiang University School of Medicine, Hangzhou. The utilization of human HCC samples and associated data was sanctioned by the Research Ethics Committee of The Second Affiliated Hospital, Zhejiang University School of Medicine, and adhered to pertinent ethical guidelines. Collection of all tissue samples was conducted in accordance with the informed consent policy. Paraffin-embedded sections of human HCC samples were immunostained with antibodies targeting PKCε pS729, ADSL pS407, INSIG1/2 scC167/C111, SREBP-1, and non-specific IgG as a negative control. The staining intensity and percentage of positive cells in the tissue sections were quantitatively evaluated as described previously[55]. The sections were assigned the following proportion scores: 0 for 0% positive staining, 1 for 0–1%, 2 for 2–10%, 3 for 11–30%, 4 for 31–70%, and 5 for 71–100%. Simultaneously, staining intensity was graded on a scale of 0–3: 0 for negative, 1 for weak, 2 for moderate, and 3 for strong. These proportion and intensity scores were then amalgamated to derive a total score within the range of 1–8 as described previously[32]. Subsequently, the acquired scores were correlated with the overall survival duration, denoting the duration from the date of diagnosis to the date of death or the last known follow-up examination. It is noteworthy that all patients had received standard post-surgery therapies.

Statistics and reproducibility

All statistical data are presented as the mean ± standard deviation (SD). All experiments, including immunoblotting, immunofluorescence, and immunoprecipitation, were repeated at least three times independently and yielded consistent results. Representative images/blots are presented. The mean values from control and experimental groups were compared for significance. Two-group comparisons were assessed using a two-tailed unpaired Student's t-test. For multiple groups or conditions, a one-way or two-way analysis of variance (ANOVA) was conducted without adjustments. For survival analysis, Kaplan–Meier curves were compared using a log-rank test. P values of less than 0.05 were considered significant. No statistical method was used to predetermine sample size. No data were excluded from the analyses. Data distribution was assumed to be normal, but this was not formally tested. Unless stated otherwise, the experiments were not randomized. Data collection and analysis were not performed blind to the conditions of the experiments. All statistical analysis was performed using GraphPad Prism 8.

Reporting summary

Further information on research design is available in the Nature Portfolio Reporting Summary linked to this article.

Data availability

Mass spectrometry data have been deposited in ProteomeXchange under accession codes PXD054753, PXD071572 and PXD074509. The UniProt protein database (EMBL-EBI) was used for protein identification. Source data are provided with this paper. The remaining data are available within the Article, Supplementary Information, or Source Data file. Source data are provided with this paper.

References

1. Faubert, B., Solmonson, A. & DeBerardinis, R. J. Metabolic reprogramming and cancer progression. *Science* https://doi.org/10.1126/science.aaw5473 (2020).
2. Hanahan, D. Hallmarks of cancer: new dimensions. *Cancer Discov.* **12**, 31–46 (2022).
3. Menendez, J. A. & Lupu, R. Fatty acid synthase and the lipogenic phenotype in cancer pathogenesis. *Nat. Rev. Cancer* **7**, 763–777 (2007).
4. Shimano, H. & Sato, R. SREBP-regulated lipid metabolism: convergent physiology - divergent pathophysiology. *Nat. Rev. Endocrinol.* **13**, 710–730 (2017).
5. Radhakrishnan, A., Ikeda, Y., Kwon, H. J., Brown, M. S. & Goldstein, J. L. Sterol-regulated transport of SREBPs from endoplasmic reticulum to Golgi: oxysterols block transport by binding to Insig. *Proc. Natl. Acad. Sci. USA* **104**, 6511–6518 (2007).
6. Osborne, T. F. & Espenshade, P. J. Evolutionary conservation and adaptation in the mechanism that regulates SREBP action: what a long, strange tRIP it's been. *Genes Dev.* **23**, 2578–2591 (2009).
7. Brown, M. S., Radhakrishnan, A. & Goldstein, J. L. Retrospective on cholesterol homeostasis: the central role of scap. *Annu. Rev. Biochem.* **87**, 783–807 (2018).
8. Goldstein, J. L., DeBose-Boyd, R. A. & Brown, M. S. Protein sensors for membrane sterols. *Cell* **124**, 35–46 (2006).
9. Guillet-Deniau, I. et al. Glucose induces de novo lipogenesis in rat muscle satellite cells through a sterol-regulatory-element-binding-protein-1c-dependent pathway. *J. Cell Sci.* **117**, 1937–1944 (2004).
10. Hasty, A. H. et al. Sterol regulatory element-binding protein-1 is regulated by glucose at the transcriptional level. *J. Biol. Chem.* **275**, 31069–31077 (2000).
11. Kaplan, M., Kerry, R., Aviram, M. & Hayek, T. High glucose concentration increases macrophage cholesterol biosynthesis in diabetes through activation of the sterol regulatory element binding protein 1 (SREBP1): inhibitory effect of insulin. *J. Cardiovasc Pharm.* **52**, 324–332 (2008).
12. Cheng, C. et al. Glucose-mediated N-glycosylation of SCAP is essential for SREBP-1 activation and tumor growth. *Cancer Cell* **28**, 569–581 (2015).

13. Toth, E. A. & Yeates, T. O. The structure of adenylosuccinate lyase, an enzyme with dual activity in the de novo purine biosynthetic pathway. *Structure* **8**, 163–174 (2000).
14. Spiegel, E. K., Colman, R. F. & Patterson, D. Adenylosuccinate lyase deficiency. *Mol. Genet Metab.* **89**, 19–31 (2006).
15. Xiao, M. et al. Inhibition of alpha-KG-dependent histone and DNA demethylases by fumarate and succinate that are accumulated in mutations of FH and SDH tumor suppressors. *Genes Dev.* **26**, 1326–1338 (2012).
16. Sulkowski, P. L. et al. Oncometabolites suppress DNA repair by disrupting local chromatin signalling. *Nature* **582**, 586–591 (2020).
17. Alderson, N. L. et al. S-(2-Succinyl)cysteine: a novel chemical modification of tissue proteins by a Krebs cycle intermediate. *Arch. Biochem. Biophys.* **450**, 1–8 (2006).
18. Adam, J. et al. Renal cyst formation in Fh1-deficient mice is independent of the Hif/Phd pathway: roles for fumarate in KEAP1 succination and Nrf2 signaling. *Cancer Cell* **20**, 524–537 (2011).
19. Humphries, F. et al. Succination inactivates gasdermin D and blocks pyroptosis. *Science* **369**, 1633–1637 (2020).
20. Kornberg, M. D. et al. Dimethyl fumarate targets GAPDH and aerobic glycolysis to modulate immunity. *Science* **360**, 449–453 (2018).
21. Thompson, C. B. et al. A century of the Warburg effect. *Nat. Metab.* **5**, 1840–1843 (2023).
22. Lee, J. H. et al. EGFR-phosphorylated platelet isoform of phosphofructokinase 1 promotes PI3K activation. *Mol. Cell* **70**, 197–210 e197 (2018).
23. Mochly-Rosen, D., Das, K. & Grimes, K. V. Protein kinase C, an elusive therapeutic target? *Nat. Rev. Drug Discov.* **11**, 937–957 (2012).
24. Parker, P. J. et al. Equivocal, explicit and emergent actions of PKC isoforms in cancer. *Nat. Rev. Cancer* **21**, 51–63 (2021).
25. Xia, P. et al. Characterization of the mechanism for the chronic activation of diacylglycerol-protein kinase C pathway in diabetes and hypergalactosemia. *Diabetes* **43**, 1122–1129 (1994).
26. Wang, Q. J. PKD at the crossroads of DAG and PKC signaling. *Trends Pharm. Sci.* **27**, 317–323 (2006).
27. Jubaidi, F. F. et al. The Role of PKC-MAPK Signalling Pathways in the Development of Hyperglycemia-Induced Cardiovascular Complications. *Int. J. Mol. Sci.* https://doi.org/10.3390/ijms23158582 (2022).
28. Chung, B. H. Y., Yeow, S. S., Chan, J. C. K. & Lee, M. Simpson-Golabi-Behmel syndrome type 1 with normal birth parameters. *BMJ Case Rep.* https://doi.org/10.1136/bcr-2021-247864 (2024).
29. Shao, W. & Espenshade, P. J. Sterol regulatory element-binding protein (SREBP) cleavage regulates Golgi-to-endoplasmic reticulum recycling of SREBP cleavage-activating protein (SCAP). *J. Biol. Chem.* **289**, 7547–7557 (2014).
30. Gong, Y., Lee, J. N., Brown, M. S., Goldstein, J. L. & Ye, J. Juxtamembranous aspartic acid in Insig-1 and Insig-2 is required for cholesterol homeostasis. *Proc. Natl. Acad. Sci. USA* **103**, 6154–6159 (2006).
31. Yan, R. et al. Structural basis for sterol sensing by Scap and Insig. *Cell Rep.* **35**, 109299 (2021).
32. Xu, D. et al. The gluconeogenic enzyme PCK1 phosphorylates INSIG1/2 for lipogenesis. *Nature* **580**, 530–535 (2020).
33. Hu, J. et al. Co-activation of AKT and c-Met triggers rapid hepatocellular carcinoma development via the mTORC1/FASN pathway in mice. *Sci. Rep.* **6**, 20484 (2016).
34. Mullen, N. J. & Singh, P. K. Nucleotide metabolism: a pan-cancer metabolic dependency. *Nat. Rev. Cancer* **23**, 275–294 (2023).
35. Pavlova, N. N., Zhu, J. & Thompson, C. B. The hallmarks of cancer metabolism: still emerging. *Cell Metab.* **34**, 355–377 (2022).
36. Li, X., Egervari, G., Wang, Y., Berger, S. L. & Lu, Z. Regulation of chromatin and gene expression by metabolic enzymes and metabolites. *Nat. Rev. Mol. Cell Biol.* **19**, 563–578 (2018).
37. Bian, X. et al. Lipid metabolism and cancer. *J. Exp. Med.* https://doi.org/10.1084/jem.20201606 (2021).
38. Sciacovelli, M. et al. Fumarate is an epigenetic modifier that elicits epithelial-to-mesenchymal transition. *Nature* **537**, 544–547 (2016).
39. Cheng, J. et al. Cancer-cell-derived fumarate suppresses the anti-tumor capacity of CD8(+) T cells in the tumor microenvironment. *Cell Metab.* **35**, 961–978 e910 (2023).
40. Xu, D. et al. The evolving landscape of noncanonical functions of metabolic enzymes in cancer and other pathologies. *Cell Metab.* **33**, 33–50 (2021).
41. Bian, X. et al. Regulation of gene expression by glycolytic and gluconeogenic enzymes. *Trends Cell Biol.* **32**, 786–799 (2022).
42. Radhakrishnan, A., Sun, L. P., Kwon, H. J., Brown, M. S. & Goldstein, J. L. Direct binding of cholesterol to the purified membrane region of SCAP: mechanism for a sterol-sensing domain. *Mol. Cell* **15**, 259–268 (2004).
43. Ren, R. et al. PROTEIN STRUCTURE. Crystal structure of a mycobacterial Insig homolog provides insight into how these sensors monitor sterol levels. *Science* **349**, 187–191 (2015).
44. Guo, D. et al. Aerobic glycolysis promotes tumor immune evasion by hexokinase2-mediated phosphorylation of IkappaBalpha. *Cell Metab.* **34**, 1312–1324 e1316 (2022).
45. Li, X. et al. Mitochondria-translocated PGK1 functions as a protein kinase to coordinate glycolysis and the TCA cycle in tumorigenesis. *Mol. Cell* **61**, 705–719 (2016).
46. Li, X. et al. Nucleus-translocated ACSS2 promotes gene transcription for lysosomal biogenesis and autophagy. *Mol. Cell* **66**, 684–697 e689 (2017).
47. Qian, X. et al. KDM3A senses oxygen availability to regulate PGC-1alpha-mediated mitochondrial biogenesis. *Mol. Cell* **76**, 885–895 e887 (2019).
48. Dimauro, I., Pearson, T., Caporossi, D. & Jackson, M. J. A simple protocol for the subcellular fractionation of skeletal muscle cells and tissue. *BMC Res. Notes* **5**, 513 (2012).
49. Zurlo, G. et al. Prolyl hydroxylase substrate adenylosuccinate lyase is an oncogenic driver in triple negative breast cancer. *Nat. Commun.* **10**, 5177 (2019).
50. Qian, X. et al. PTEN suppresses glycolysis by dephosphorylating and inhibiting autophosphorylated PGK1. *Mol. Cell* **76**, 516–527 e517 (2019).
51. Gad, H. et al. MTH1 inhibition eradicates cancer by preventing sanitation of the dNTP pool. *Nature* **508**, 215–221 (2014).
52. Lavinder, J. J., Hari, S. B., Sullivan, B. J. & Magliery, T. J. High-throughput thermal scanning: a general, rapid dye-binding thermal shift screen for protein engineering. *J. Am. Chem. Soc.* **131**, 3794–3795 (2009).
53. Danai, L. V. et al. Map4k4 suppresses Srebp-1 and adipocyte lipogenesis independent of JNK signaling. *J. Lipid Res.* **54**, 2697–2707 (2013).
54. Li, X. et al. A splicing switch from ketohexokinase-C to ketohexokinase-A drives hepatocellular carcinoma formation. *Nat. Cell Biol.* **18**, 561–571 (2016).
55. Yang, W. et al. Nuclear PKM2 regulates beta-catenin transactivation upon EGFR activation. *Nature* **480**, 118–122 (2011).

Acknowledgements

This study was supported by grants from the Ministry of Science and Technology of the People's Republic of China (2021YFA0805600, D.X.; 2020YFA0803300, Z.L.; 2023YFC2606500, P.Z.), the National Natural Science Foundation of China (82188102, 82030074, Z.L.; 82525043, U25A20112, 32470815, D.X.; 82372814, 82573010, Z.W.), the Zhejiang Natural Science Foundation Key Project (LR25H160003, LD22H160002, D.X.; LR26H160003, Z.W., LD21H160003, Z.L.), Zhejiang Natural Science Foundation Discovery Project (LQ22H160023, Z.W.), High-Level Talent Special Support Programs of Zhejiang Province-Young Talents (588020-

X42402, X42502, Z.W.), Key Research and Development Program, Ministry of Science and Technology of the People's Republic of China (Grant No. 2023YFC2606500). The author gratefully acknowledges the support of K.C. Wong Education Fundation.

Author contributions

Z.W., P.Z., S.L., and D.X. conceived and designed the study. Z.W., D.X., P.Z., and Z.L. acquired funding support and supervised the study. Y.D., J.L., W.Q,. and Y.S. performed the experiments and analyze the data, including cell biology and biochemical experiments. S.W. and P.Z. were involved in MD simulation analyses. Y.D., Y.H., X.S., Y.L., Z.H., and B.D. performed the experiments and analyze the data (animal studies). Y.D., Y.B., H.Y., M.L., L.X., and Q.W. checked and revised the manuscript. Y.D. and D.X. wrote the paper integrating comments from all other authors. T.L., Y.L., Z.M., Y.D., G.L., Y.W., and X.B. provided technical support and reviewed the paper.

Competing interests

The authors declare no competing interests.

Additional information

Supplementary information The online version contains supplementary material available at https://doi.org/10.1038/s41467-026-70583-0.

Correspondence and requests for materials should be addressed to Daqian Xu, Shijian Liu, Peng Zhan or Zheng Wang.

Peer review information *Nature Communications* thanks Esteban Gurzov, who co-reviewed with Eduardo Gilglioni, and the other anonymous reviewer(s) for their contribution to the peer review of this work. A peer review file is available.

[1]Zhejiang Provincial Key Laboratory of Pancreatic Disease, The First Affiliated Hospital, Institute of Translational Medicine, Zhejiang University School of Medicine, Zhejiang University, Hangzhou, China. [2]Zhejiang Key Laboratory of Frontier Medical Research on Cancer Metabolism, Hangzhou, China. [3]Department of Hepatobiliary and Pancreatic Surgery, The Second Affiliated Hospital, Zhejiang University School of Medicine, Hangzhou, Zhejiang, China. [4]Key Laboratory of Precision Diagnosis and Treatment for Hepatobiliary and Pancreatic Tumor of Zhejiang Province, Hangzhou, Zhejiang, China. [5]Department of Medicinal Chemistry, Key Laboratory of Chemical Biology, Ministry of Education, School of Pharmaceutical Sciences, Shandong University, Jinan, Shandong, China. [6]Department of Oncology Surgery, Harbin Medical University Cancer Hospital, Harbin, China. [7]NHC Key Laboratory of Cell Transplantation, Harbin Medical University, Harbin, China. [8]Phase I Clinical Trial Center, Department of Medical Oncology, Shanghai Medical College, Fudan University Shanghai Cancer Center, Shanghai, China. [9]Department of Oncology, Shanghai Medical College, Fudan University, Shanghai, China. [10]Department of Medical Oncology, Fudan University Shanghai Cancer Center Xiamen Hospital, Xiamen City, Fujian Province, China. [11]MOE Key Laboratory of Macromolecular Synthesis and Functionalization, Department of Polymer Science and Engineering, Zhejiang University, Hangzhou, Zhejiang, China. [12]Department of Colorectal Surgery and Oncology of the Second Affiliated Hospital and Institute of Translational Medicine, Zhejiang University School of Medicine, Hangzhou, China. [13]Department of Laboratory Medicine, Chongqing General Hospital, School of Medicine, Chongqing University, Chongqing, China. [14]These authors contributed equally: Yuran Duan, Shuo Wang, Jianyu Liu, Wenxing Qin, Yuli Shen. ✉e-mail: xudaqian@zju.edu.cn; liushijian@hrbmu.edu.cn; zhanpeng1982@sdu.edu.cn; wangzheng22@zju.edu.cn